Free Radical Biology and Medicine 197 (2023) 71–84

Contents lists available at ScienceDirect

Free Radical Biology and Medicine

journal homepage: www.elsevier.com/locate/freeradbiomed

Redox sensitive human mitochondrial aconitase and its interaction with frataxin: *In vitro* and *in silico* studies confirm that it takes two to tango

Santiago Mansilla [a,b], Verónica Tórtora [a,c], Florencia Pignataro [d], Santiago Sastre [a,e], Ignacio Castro [d], Ma. Laura Chiribao [a,f,g], Carlos Robello [a,f,g], Ari Zeida [a,f], Javier Santos [d,**], Laura Castro [a,f,*]

[a] Centro de Investigaciones Biomédicas, Facultad de Medicina, Universidad de la República, Montevideo, Uruguay
[b] Departamento de Métodos Cuantitativos, Facultad de Medicina, Universidad de la República, Montevideo, Uruguay
[c] Departamento de Educación Médica, Facultad de Medicina, Universidad de la República, Montevideo, Uruguay
[d] Instituto de Biociencias, Biotecnología y Biología traslacional, Facultad de Ciencias Exactas, Universidad de Buenos Aires, Buenos Aires, Argentina
[e] Departamento de Biofísica, Facultad de Medicina, Universidad de la República, Montevideo, Uruguay
[f] Departamento de Bioquímica, Facultad de Medicina, Universidad de la República, Montevideo, Uruguay
[g] Laboratorio de Interacciones Hospedero-Patógeno, Institut Pasteur de Montevideo, Uruguay

ARTICLE INFO

Keywords:
Mitochondrial aconitase
Frataxin
Iron-sulfur protein
Tricarboxylic acid cycle (TCA cycle) (Krebs cycle)
Mitochondria
protein-protein interaction

ABSTRACT

Mitochondrial aconitase (ACO2) has been postulated as a redox sensor in the tricarboxylic acid cycle. Its high sensitivity towards reactive oxygen and nitrogen species is due to its particularly labile $[4Fe–4S]^{2+}$ prosthetic group which yields an inactive $[3Fe–4S]^{+}$ cluster upon oxidation. Moreover, ACO2 was found as a main oxidant target during aging and in pathologies where mitochondrial dysfunction is implied.

Herein, we report the expression and characterization of recombinant human ACO2 and its interaction with frataxin (FXN), a protein that participates in the *de novo* biosynthesis of Fe–S clusters.

A high yield of pure ACO2 (≥99%, 22 ± 2 U/mg) was obtained and kinetic parameters for citrate, isocitrate, and *cis*-aconitate were determined. Superoxide, carbonate radical, peroxynitrite, and hydrogen peroxide reacted with ACO2 with second-order rate constants of 10^8, 10^8, 10^5, and 10^2 M^{-1} s^{-1}, respectively. Temperature-induced unfolding assessed by tryptophan fluorescence of ACO2 resulted in apparent melting temperatures of 51.1 ± 0.5 and 43.6 ± 0.2 °C for $[4Fe–4S]^{2+}$ and $[3Fe–4S]^{+}$ states of ACO2, sustaining lower thermal stability upon cluster oxidation. Differences in protein dynamics produced by the Fe–S cluster redox state were addressed by molecular dynamics simulations.

Reactivation of $[3Fe–4S]^{+}$-ACO2 by FXN was verified by activation assays and direct iron-dependent interaction was confirmed by protein-protein interaction ELISA and fluorescence spectroscopic assays. Multimer modeling and protein-protein docking predicted an ACO2-FXN complex where the metal ion binding region of FXN approaches the $[3Fe–4S]^{+}$ cluster, supporting that FXN is a partner for reactivation of ACO2 upon oxidative cluster inactivation.

1. Introduction

Mitochondrial aconitase (ACO2, EC 4.2.1.3) is an essential enzyme that participates in the tricarboxylic acid cycle (TCA), catalyzing the reversible isomerization from citrate to isocitrate through a *cis*-aconitate intermediate in a non-redox reaction. This 83 kDa protein contains a cubane iron-sulfur cluster $[4Fe–4S]^{2+}$ ligated to three protein cysteines by iron-sulfur covalent bonds while the fourth iron, termed Fe_{α}, is linked only to inorganic sulfur atoms and can bind oxygen atoms from its substrates or water [1,2]. The integrity of the $[4Fe–4S]^{2+}$ cluster is essential for catalysis.

Mitochondrial $[4Fe–4S]^{2+}$ cluster aconitase evolves from α-proteobacteria aconitate hydratase B (AcnB) which is extremely sensitive to oxygen and oxygen-derived reactive species. These include ROS such as

* Corresponding author. Centro de Investigaciones Biomédicas, Facultad de Medicina, Universidad de la República, Montevideo, Uruguay.
** Corresponding author.
E-mail addresses: javiersantosw@gmail.com (J. Santos), lcastro@fmed.edu.uy (L. Castro).

https://doi.org/10.1016/j.freeradbiomed.2023.01.028
Received 6 December 2022; Received in revised form 11 January 2023; Accepted 30 January 2023
Available online 3 February 2023

superoxide anion ($O_2^{\bullet-}$), hydrogen peroxide (H_2O_2), hydroxyl radical ($^{\bullet}OH$), and reactive species derived from ROS reactions with nitric oxide ($^{\bullet}NO$) such as peroxynitrite ($ONOO^-$), carbonate radical ($CO_3^{\bullet-}$), and nitrogen dioxide ($^{\bullet}NO_2$) [3]. In fact, ACO2 is extremely sensitive to $O_2^{\bullet-}$ inactivation being one of the few direct targets of this radical, reacting with fast second-order rate constants ranging from 10^6 to 10^8 M^{-1} s^{-1} and yielding a catalytic inactive $[3Fe–4S]^+$ cluster [4,5]. ACO2 can also react with $^{\bullet}NO$, $ONOO^-$, $CO_3^{\bullet-}$, and $^{\bullet}NO_2$ [6,7]. The presence of oxidized and nitrated ACO2 in several animal models of sepsis, inflammation, aging, and diabetes, reveals the enzyme as an important target of nitroxidative species [8–10].

In normal mammalian cell intermediary metabolism, ACO2 is typically present in excess and catalyzes a reaction that results in a characteristic approximately citrate:isocitrate ratio of 10:1 ($\Delta G^{\circ\prime} = 6.3$ kJ/mol), for most mammalian tissues [11]. Despite not being classically considered a key regulator of TCA, using a limited metabolic control analysis in isolated mitochondria from rat tissues, we showed that inhibition of aconitase could impact mitochondrial metabolism by diminishing the entry of reducing equivalents to the electron transport chain (ETC), decreasing mitochondrial membrane potential, and slowing the rate of $O_2^{\bullet-}$ and H_2O_2 production [12]. These observations support the hypothesis that ACO2 acts as a redox rheostat, regulating the levels of $O_2^{\bullet-}$ generated by the ETC and tuning metabolism by channeling citrate either for the production of NADH for energy metabolism or diverting it to the cytosol for the synthesis of fats or acetylation reactions [13].

In this regard, besides being a key constituent of the TCA cycle, citrate is an excellent chelating agent for divalent cations, also serves as a substrate for fatty acid and sterol biosynthesis, and functions as a key regulator of intermediary energy metabolism. Specialized tissues modulate ACO2 activity to accumulate and export citrate for other cells. For instance, normal prostate glands accumulate high Zn^{2+} levels, resulting in the inhibition of ACO2 and in a shift of its equilibrium towards citrate, which is exported to being part of the prostatic fluid [14–16]. Other specialized cells specifically synthesize and export citrate, as is the case of astrocytes. The ability of astrocytes to produce large amounts of citrate may be reflected in its relatively high concentration (0.4 mM) found in cerebrospinal fluid, similar to the level of glutamine considered a main neuron metabolic substrate [17]. Also, abundant data support that citrate may also play an important role in other key biological processes such as inflammation, cancer, insulin secretion, histone acetylation, and non-alcoholic fatty acid liver [18].

Oxidized $[3Fe–4S]^{+}$-ACO2 is reactivated *in vivo* by reconstitution of the $[4Fe–4S]^{2+}$ cluster by Fe^{2+} in the presence of intra-mitochondrial reductants such as glutathione [19]. Reversible inactivation is necessary to function as a redox sensor. Possible protein partners that facilitate the reactivation process were postulated. In this regard, in 2004 it was postulated that frataxin (FXN), a protein that participates in the *de novo* biosynthesis of Fe–S clusters, was involved in repairing oxidatively inactivated $[3Fe–4S]^{+}$-ACO2 [20].

FXN is a 14.3 kDa protein that has been shown to work as a kinetic activator of L-Cys desulfurase NFS1 supercomplex for the [2Fe–2S] cluster assembly [21–23] and also as an iron chaperone as it possesses several coordination sites for metal ions [24]. In this subject, it was shown that bacterial FXN can specifically bind iron by using its "acidic ridge", a region of the protein rich in the acidic residues Glu and Asp involving alpha helix 1, loop 1, and beta strand 1. NMR chemical shift perturbation studies using ^{15}N-labeled FXN allowed to assign the residues involved in the iron binding [25]. Furthermore, yeast FXN was also stable as the iron-loaded monomer and the protein were able to bind two Fe^{2+} atoms per FXN monomer with micromolar binding affinity, and the residues affected by the presence of iron were located within the conserved acidic ridge [26]. Moreover, human FXN also exhibited iron binding capability with both Fe^{2+} and Fe^{3+} [27]. However, Fe^{2+} induced larger shifts or a higher intensity decrease of the NMR signals, except for residues 119 and 120, which appear more shifted upon addition of Fe^{3+}. In the same fashion, EPR experiments unequivocally showed that FXN was able to bind Fe^{3+} [27]. Additionally, the grafting of the *EExxED* motif on peptide and protein models generated an iron binding site [28]. This motif is present in the acidic ridge of the FXN protein family. Remarkably, Cai and coworkers showed by means of NMR spectroscopy that the complex Fe^{2+}-FXN binds to the mammalian NFS1/ACP-ISD11/ISCU2 complex without the release of iron. After the addition of both L-Cys and a reductant agent (either reduced FDX2 or DTT), iron is released from FXN [29].

Data regarding ACO2 and FXN interactions was sustained by ACO2 immunoprecipitation following H_2O_2 exposure to mitochondria from either *Saccharomyces cerevisiae* or rat hearts, which rendered FXN as an associated protein [20]. Nevertheless, co-immunoprecipitation of FXN with ACO2 could not be reproduced by others, even when ISCU, NFS1, ISD11, and MPP (other protein members of the Fe–S machinery synthesis) were present, therefore confronting the hypothesis of direct ACO2-FXN interaction during ACO2 reactivation [30,31].

Current biochemical and structural data in mammalian ACO2 were performed using pig or bovine protein and until now data regarding *in vitro* data for human ACO2 is missing.

The present study describes the novel expression, purification, and characterization of recombinant human ACO2, including kinetics, oxidant reactivity, structural studies, and present evidence for its direct interaction with human FXN. This work confirmed that FXN acts as a protein partner of ACO2 not only during Fe–S maturation but also during the oxidative inactivated $[3Fe–4S]^{+}$-ACO2 repairing, supporting data of highly compromised ACO2 activity in Friedreich's Ataxia in human, animal and cellular disease models, which may be the result of both the decrease of Fe–S cluster biosynthesis and the decrease in ACO2 activation processes.

2. Materials and methods

2.1. Materials

Chemical compounds were purchased from Sigma Chemical CO. (St. Louis, MO) unless otherwise specified. Peroxynitrite was synthesized as described in Ref. [32]; when used, it was diluted in freshly prepared 5 mM NaOH.

Antibodies: anti-Mitochondrial aconitase (ab71440) was obtained from Abcam (Cambridge, UK). anti-Rabbit antibody (IRDye 800 CW) was acquired from Li-Cor (Lincoln, Nebraska, USA). Nitrogen and argon were acquired from AGA (Montevideo, Uruguay). Anti-FXN rabbit serum was produced in the laboratory of Dr. Javier Santos as described in Ref. [33].

All solutions were prepared using distilled deionized water (Barnstead Smart2Pure).

2.2. Construction of ACO2 expression system

Primers for amplification were designed using the Primer3Plus online tool [34], based on the mature human ACO2 gene sequence obtained from GenBank (ID: CR536568.1). The forward primer (5′-TAAGCAgctagcCAACGGGCCAAGGTGGCGAT-3' [restriction -site for NheI in lower cases]) and reverse primer (5′-TGCTTGaagcttTCACTGTTGCAGTTCCTTCA-3' [restriction site for Hind III]) were purchased from IDT (Coralville, Iowa, USA). The gene was cloned from cDNA of Thp1 cell line (human monocytic cell) into a pGEM -T vector (Promega, US) using commercial kits (Thermo Fisher, Massachusetts, USA) and amplified in *E. coli* TOP10 electrocompetent cells. The plasmid containing ACO2 was double digested with NheI and HindIII and the amplicon was ligated in a pET28(c)+ expression plasmid (HIS-tag and kanamycin resistance), and later used for transformation of *E. coli* BL21 (DE3) electrocompetent cells. Expression plasmid was sequenced to verify integrity at the Sequencing Service from the Institut Pasteur de Montevideo, Montevideo, Uruguay.

2.3. Expression and purification of ACO2

E. coli BL21(DE3) cells, harboring the ACO2 expression system were grown using a temperature-controlled shaker at 220 rpm, for 18 h at 37 °C in flasks containing 25 mL of LB medium supplemented with kanamycin (30 μg/mL). The flasks were used as an inoculum for flasks with 1 L of the same media. Cultures were grown in the same conditions until reaching an optical density of 0.5–1.0 at 600 nm and then IPTG 0.5 mM was added for induction. The expression under various conditions was tracked by SDS-PAGE and optimal growth conditions were determined (25 °C for 18 h).

2.4. Mitochondrial aconitase purification

Cells were harvested by centrifugation at 4,500 g for 20 min at 4 °C and then resuspended in PBS, containing 0.1 mM phenylmethanesulfonyl fluoride (PMSF) and 0.1 mg/mL of DNAse. The cell suspension was lysed by sonication and later cleared by centrifugation at 15,000 g for 20 min at 4 °C and filtration. HIS-tagged-ACO2 was purified from the supernatant by immobilized metal affinity chromatography (IMAC) using a 5 mL Hi-Trap column (GE Healthcare, Illinois, USA) following the manufacturer's instructions. The protein was eluted using an imidazole gradient and then dialyzed against a 50 mM Tris buffer containing 100 mM NaCl, pH 7.8. On a second purification step, ACO2 was separated from contaminants by using size exclusion chromatography on a PD-10 column packed with Sephadex G-25 resin. Protein purity was assessed by SDS-PAGE and mass spectrometry. ACO2 could also be visually followed by its brownish color characteristic of iron-sulfur proteins. HIS-tag was cleaved with thrombin and removed by filtration and the purified ACO2 was changed to a pH 7.8 HEPES buffer, 100 mM NaCl and 2 mM DTT. Protein was centrifuged at 15,000 g for 20 min at 4 °C to pellet aggregated protein and the final concentration was assayed by Bradford's method using bovine serum albumin as standard. Purified ACO2 was stored at −80 °C until use. ACO2 purity was assayed by SDS-PAGE.

2.5. Aconitase activation and activity measurements

As ACO2 is inactivated by oxygen during purification [35], the enzyme was reactivated by incubation with 100 μM ferrous ammonium sulfate ($(NH_4)_2Fe(SO_4)_2$) and 10 mM dithiothreitol (DTT) to a final volume of 1.0 mL in a 25 mM Tris-HCl buffer containing 100 mM NaCl pH 7.4 for 1 h under an argon saturated atmosphere on an anaerobic vial. Different volumes of activated ACO2 were withdrawn from the anaerobic vial using gas-tight syringes (Hamilton) and added to a cuvette containing substrates in Tris-HCl buffer. Aconitase activity was measured using the three substrates of the enzyme: citrate, isocitrate, and *cis*-aconitate by following the double bond of *cis*-aconitate by absorbance at 240 nm ($\varepsilon = 3.6\ mM^{-1}\ cm^{-1}$) [35]. Activation and activity measurements were performed at 25 °C. Activation in the presence of 500 μM sodium disulfide did not show higher activity, implying that purified ACO2 is mainly obtained in the $[3Fe–4S]^+$ form and not as apo-ACO2. Activity measurements as well as spectra determination were carried out with a Shimadzu UV–Vis spectrophotometer UV-2450.

2.6. Reactions constants with oxidants

Excess iron and DTT added during ACO2 activation were removed by Sephadex G-25 gel filtration carried on a hypoxic chamber (Coy Instruments) under a nitrogen atmosphere and O_2 level below 2%. Purified ACO2 was collected on anaerobic vials and oxidants were added also in hypoxia. Different approaches were used for the determination of the constant at 25 °C with each oxidant. ACO2 concentration used was in the range of 0.4–2 μM.

For $ONOO^-$, active ACO2 was diluted in a 100 mM Tris, pH 7.6 buffer previously degassed, aliquoted, and then different concentrations of $ONOO^-$ were added in bolus and vortexed. Effects of contaminants from the $ONOO^-$ synthesis (H_2O_2) or stable products from the $ONOO^-$ decomposition were discarded by a reverse addition assay where $ONOO^-$ is incubated in the buffer for its decomposition before adding ACO2. Aconitase activity was assayed for determining residual activity. The reaction constant was obtained by comparing experimental data against simulated data as reaction constants for decomposition and other reactions involving $ONOO^-$ are already known [10].

For $CO_3^{\bullet-}$, active ACO2 was treated as with $ONOO^-$ in presence of 25 mM HCO_3^-. Under these conditions, the CO_2 concentration is calculated to be 1.5 mM, similar to the physiological mitochondrial CO_2 concentration. To determine the rate constant for the reaction we followed the same approach used for $ONOO^-$. We performed computer-assisted simulations of ACO2 activity in the presence of CO_2 and different concentrations of $ONOO^-$ (0–5 μM), varying the value of the second-order rate constant for the reaction between $CO_3^{\bullet-}$ and ACO2.

For H_2O_2, active ACO2 was exposed to different concentrations of H_2O_2 in anaerobic vials and the loss of ACO2 activity was followed in time by withdrawing aliquots and measuring the consumption of *cis*-aconitate at 240 nm as described above. H_2O_2 was diluted from stock immediately before use and dilution concentration was determined by absorbance at 240 nm ($\varepsilon = 43.6\ M^{-1}\ cm^{-1}$ [36]).

To determine the reaction constant of ACO2 with $O_2^{\bullet-}$ a competition assay with superoxide dismutase (CuZnSOD) was used following the procedure proposed in Ref. [6]. Briefly, active ACO2 was exposed to a $O_2^{\bullet-}$ flux produced by a xanthine oxidase (0.65 mU) in presence of xanthine (150 μM). The competition of ACO2 and SOD for $O_2^{\bullet-}$ was evaluated in presence of catalase (0.5 μM). Under these conditions the next equation is valid:

$$\frac{F[A]}{(1-F_i)k_s} = \frac{1}{k_d}[C] \qquad \text{Eq.1}$$

Being F the proportion of inhibited ACO2 at a certain competitor's concentration and k_s and k_d the reaction constant of the $O_2^{\bullet-}$ with the competitor and ACO2 respectively. Here, k_s has already been reported to be $2 \times 10^9\ M^{-1}\ s^{-1}$ [37].

2.7. Molecular modeling methods

The structure of the human ACO2 has not been solved to date but it shares a high amino acid sequence identity (97%) with the pig ACO2 whose structure is available (PDB ID:6ACN). 24 punctual mutations were applied to the pig ACO2 with the FoldX [38] plugin in the YASARA View [39] software. The six amino acids from the His-tag cleavage (5′-GSHMAS-3′) were added to the model. The system was embedded in a truncated octahedral TIP3P water box [40] of 106 × 106 × 106 Å dimensions. All used residue parameters correspond to the parm99 Amber force field, except for the iron-sulfur cluster and the substrates. Parameters for the iron-sulfur cluster were developed based on work from Carvalho, A., et al. [41] (Figure S-1), while those for the substrates were developed by a standard RESP procedure. Briefly, substrate structures were optimized in an implicit water solvent at the B3LYP/6-31G* level of theory and partial charges were computed using the restricted electrostatic potential at the HF/6-31G* level of theory. Equilibrium distances and angles, as well as force constants, were computed using the same methods and basis set used for computed charges. All electronic structure calculations were performed using Gaussian09 [42].

Molecular dynamics (MD) simulations were performed using a 9 Å cutoff and particle mesh Ewald (PME) summation method for treating the electrostatic interactions. The hydrogen bond lengths were kept at their equilibrium distances by using the SHAKE algorithm, while temperature and pressure were kept constant with a Langevin thermostat and barostat, respectively, as implemented in the AMBER18 program [43]. The system was minimized, heated from 0 to 300 K (20 ps), and equilibrated (0.2 ns). After these steps, 3 to 6 replicates of a 1 μs long MD

simulation at constant temperature (300 K) and pressure (1 bar) were performed for both, active ($[4Fe–4S]^{2+}$) and inactive ($[3Fe–4S]^{+}$) ACO2. Analysis was performed by including all data from different replicates.

In order to estimate the pKa of the catalytic His101, we also applied a constant pH molecular dynamics approach [44]. pH titration curves were obtained by applying the following protocol [45]: 10 ns long simulations at constant pH were performed from pH 4 to 14, with a step of 0.2 pH units (500 ns total). Between pH 8 and 9, steps were reduced to 0.1 pH units and 5 ns to better sample the inflection point. During simulation, in each frame (timestep = 2 ps), the protonation state of the residue was selected by Monte Carlo sampling based on calculated energy differences between the possible protonation states. The protonated fraction in each pH step was calculated by dividing the number of frames with the protonated residue by the total number of frames.

ACO2 opening motion was followed by measuring the angle between the mass centers of two residue groups located in highly rigid antiparallel beta sheets: group 1 located in domain 3 (Arg351, Val352, Gly353, Thr440, Ile441, Val442, His460, Ala461, Phe462) and group 2 located in domain 4 (Leu558, Ile559, K560, Val631, Val632, Ile633, Ala658, Ile659, Ile660), using the Fe–S cluster as the angle vertex.

Binding free energy calculations were performed at the MM/GBSA level [46] for the simulations with substrates at the active site. Initial models were created by using the information of substrate-like molecules at the active site of pig ACO2 (PDB ID: 6ACN). Initially, a series of harmonic restraints designed based on experimental data [47] were applied to maintain substrate positions (Figure S-2). After minimizing and equilibrating, and allowing the binding mode of the substrate to adjust their conformations smoothly, the force constants of the harmonic restraints were gradually turned off (from k = 50 kcal/mol to 0), during a 500 ns long MD simulation.

Analyses were performed using the cpptraj [48] module of AMBER18 and bio3d R package (v2.4–3) [49]. Structural visualization was done with VMD 1.9.4 [50].

2.8. Frataxin production and purification

Mature version of human frataxin (residues 90–210) and mutant H177C were expressed and purified as described previously [51]. Briefly, transformed *E. coli* BL21(DE3) were grown in Terrific Broth, pH 7.5 culture media at 37 °C and 280 rpm. Protein expression was induced at DO = 1.0 by the addition of 1.0 mM IPTG and induced for 3.5 h at the same temperature. Cells were disrupted and FXN was purified by ion-exchange chromatography (DEAE DE52 matrix), followed by exclusion chromatography on a preparative Sephadex G-100 column (SEC, 93 cm × 2.7 cm). Purified FXN concentration was determined spectroscopically using an extinction coefficient ε_{280} = 26,930 M^{-1} cm^{-1}. FXN mutant H177C was labeled with Texas Red maleimide dye (Thermo Fisher) as previously described [52].

2.9. Protein-protein interaction ELISA

ELISA was carried out following the procedure described in Ref. [53]. Briefly, ACO2 5 μg/mL was immobilized by noncovalent coating onto the wells of a 96-well microtiter plate at 100 μL/well in a buffer containing 100 mM KCl, 3 mM $MgCl_2$, and 10 mM PIPES, pH 7.0 (buffer A). Plate was sealed and incubated at 4 °C overnight and then washed to remove unbound protein and blocked by adding buffer A with 0.1% Tween-20 and 0.1% BSA (buffer B) for 1 h at room temperature. The plate was washed three times with buffer A containing 0.1% Tween-20 (buffer T). After this step, serial dilutions of FXN or BSA as control were added to the wells at 100 μL/well and incubated with the immobilized ACO2 for 2 h at room temperature under air and in presence of 200 μM Fe^{2+} and 10 mM DTT. Following this incubation, the plate was washed again three times with buffer T and the FXN or BSA bound to immobilized ACO2 were detected using an anti-FXN rabbit serum and an anti-rabbit IgG bound to HRP at a previously optimized dilution. Finally, the assay was revealed at 450 nm using the chromogenic substrate OPD (o-phenylenediamine dihydrochloride) following manufacturer guidelines (P-3804, Sigma-Aldrich).

2.10. Fluorescence analysis

Thermal denaturation spectrums were performed in an FP-8500 fluorescence spectrometer (Jasco Inc.). For the Trp fluorescence, the excitation wavelength was fixed at 295 nm, and the emission spectrum was recorded from 305 to 400 nm, while for 1-anilino-8-naphthalene sulfonate (ANS), samples were excited at 380 and scanned from 400 to 600 nm. Slits of 2.5 nm in the excitation and emission paths were used with a 1-cm path length quartz cuvette. The Trp relative fluorescence was obtained by dividing the area for each temperature by the fluorescence at 20 °C.

Anisotropy fluorescence measurements were performed on an FP-8300 fluorescence spectrometer with an automatic polarizer (Jasco Inc.). Excitation and emission slits were adjusted to 10 nm to maximize intensity counts. The concentration of Texas Red-labeled FXN was adjusted to 5.0 μM. Excitation was done at 590 and emission data were collected at 615 nm. Experiments were performed at 15 °C and the temperature during measurements was maintained using a thermoregulated Peltier. The fluorescence anisotropy (r) was calculated using the following equation:

$$r = \frac{I_{vh} - GI_{vh}}{I_{vv} - 2GI_{vh}}, \quad \text{Eq.2}$$

where I_{vv} is the intensity of the detected light with both excitation and emission polarizers mounted vertically, I_{vh} is the intensity of the detected light with the excitation polarizer installed vertically and the emission polarizer mounted horizontally. The factor G in equation (2) for each sample was determined by measuring the intensities of the detected lights, I_{hv} and I_{hh}, with the emission polarizer installed horizontally and vertically, respectively, under the excitation polarizer mounted horizontally and calculating $G = I_{hv}/I_{hh}$ [54]. Under the assumption of only 1 binding site for the interaction of FXN and ACO2, the curves of anisotropy titration with ACO2 were fitted using:

$$r_{obs} = r_0 + \frac{\Delta r_{PL}[ACO2]_T}{K_d + [ACO2]_T}, \quad \text{Eq.3}$$

where r_{obs} corresponds to the observed anisotropy value, r_0 is the initial anisotropy value of the free Texas Red-labeled FXN, $[ACO2]_T$ is the total concentration of ACO2, K_d corresponds to the dissociation constant for the binding event and Δr_{PL} corresponds to $(r_{PL} - r_P)([FXN]_T)$, being r_{PL} and r_P the anisotropy values of the complex and ACO2 and $[FXN]_T$ the total concentration of Texas Red-labeled FXN [55]. Before use, all solutions were centrifuged for 20 min at 15,000 g to sediment light-scattering particles.

2.11. Docking experiments

First, initial complex models for the interaction of ACO2 and FXN were predicted with the AlphaFold2-multimer algorithm [56], while sequence alignments were generated with MMseqs2 and HHsearch [56]. Query sequences were designed based on references for the human ACO2 (UniProt Q99798) and the human FXN 90–210 (UniProtQ16595). The acidic ridge of FXN, a region rich in Glu and Asp (original sequence "90-L**D**E**T**T**Y**E**R**LA**E**E**T**L**D**SL-117") was mutated to "90-L**AA**T**T**Y**A**R-LA**AA**T**A**L**A**SL-117" in the queries for AlphaFold prediction.

Then, docking experiments of ACO2 and FXN were performed in HADDOCK 2.4 [57,58] using the structures obtained from the MD simulation for the active and inactive ACO2 and the crystal structure of human FXN (PDB ID:1EKG). Selected active residues were residues 90 to 117 and residues located in the ACO2 cleft formed by the domains 3 and

4 (166, 167, 201, 218, 221–235, 258–265, 322–332, 337, 340, 344, 346, 424, 425, 443, 445–453, 455–463, 559–573, 589–604, 632–644, 647, 651, 659–669, 672, 681, 682, 685, 688, 589). The docking solutions were evaluated based on the HADDOCK score and the Z-score (the number of standard deviations the HADDOCK score of a given cluster is separated from the mean of all clusters).

2.12. Statistical analysis

Plots and statistical analysis were performed using GraphPad Prism 8.0. P values < 0.05 were considered statistically significant and indicated with asterisks in graphs (*P < 0.05, **P < 0.01, ***P < 0.001, ns not significant). Means were compared using Welch's *t*-test.

All relevant data used for running experiments, model fitting, and plotting is available on a GitHub repository at (https://github.com/smansilla16/Mansilla-S_2022). This article contains supplementary material.

3. Results

3.1. Biochemical characterization of ACO2

Recombinant human ACO2 was expressed with a high yield (20 mg/L) and purity (>99%) and its molecular weight was determined by mass spectrometry (83,002 ± 6 Da being the theoretical molecular weight 82,996 Da) (Figure S-3).

Reactivated ACO2 was used to study the kinetic constants for its substrates (citrate, *cis*-aconitate, and isocitrate). ACO2 exhibited Michaelis-Menten (MM) kinetics for its three substrates, therefore the MM constant (K_M), turnover number (k_{cat}) and catalytic efficiency (k_{cat}/K_M) were determined by fitting the MM equation to experimental data (Fig. 1).

Obtained catalytic efficiencies differed by an order of magnitude between citrate, isocitrate, and *cis*-aconitate (10^4, 10^5, and 10^6 s^{-1} M^{-1}) mainly because of the differences in K_M (Table 1). These results were compared with the binding energy of the substrate for the active site of ACO2 obtained from molecular dynamic simulations (see below in Fig. 6).

Freshly obtained ACO2 from purification presented a brownish color, as reported for other Fe–S proteins, and did not have activity as the $[4Fe–4S]^{2+}$ is inactivated by molecular oxygen. To verify the status of the Fe–S cluster, we activated ACO2 with 100 μM Fe^{2+} and in the presence or absence of Na_2S under an Ar-saturated atmosphere. As previously verified for other mammalian aconitases, when incubating the apo-ACO2 with Fe^{2+} and S^{2-}, the $[4Fe–4S]^{2+}$ can be reconstituted [62]. As shown in Fig. 2A, no difference in activation was observed

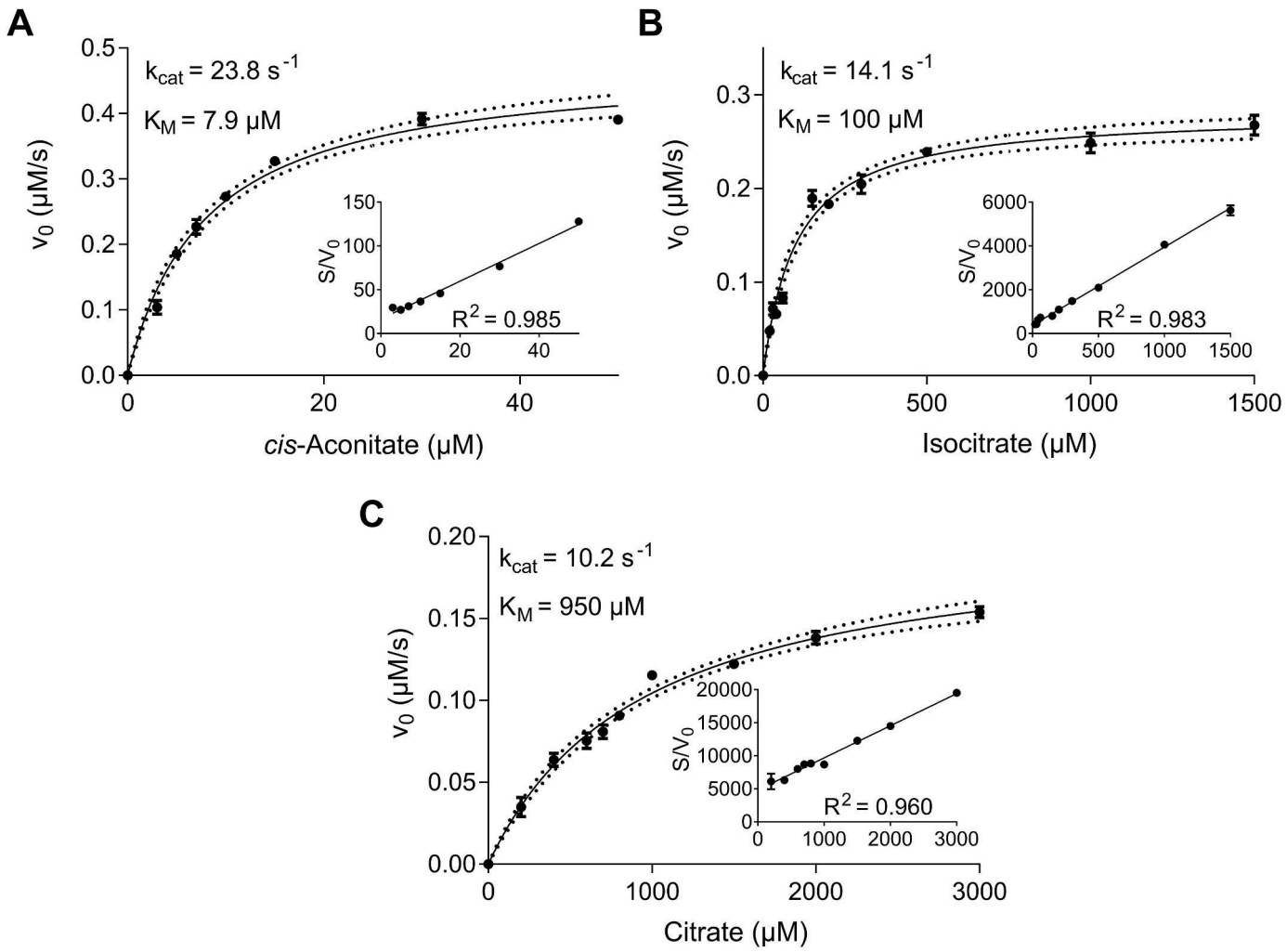

Fig. 1. *Michaelis-Menten parameters of ACO2.* Aliquots of active ACO2 were withdrawn from an anaerobic vial and added to a substrate-containing quartz cuvette to a final volume of 1 mL. Reactions were followed spectrophotometrically by measuring consumption or formation of *cis*-aconitate (ε_{240} = 3,6 mM^{-1} cm^{-1}) at different concentrations of substrates for 1 min: A) *cis*-aconitate, B) isocitrate, C) citrate. The activity was measured in a 20 mM HEPES buffer, pH 7.8, containing 150 mM NaCl using 20 nM ACO2. MM equation was fitted to experimental data. The dotted line represents the 95% confidence band of the fitting. Hanes and Woolf's linearization (S/v_0 vs. S) and its coefficient of determination (R^2) are shown in the inset for validation.

Table 1
Kinetic parameters of human ACO2.

Substrate	K_M (μM)	k_{cat} (sec^{-1})	k_{cat}/K_M (sec^{-1} M^{-1})	Organism	Reference
cis-Aconitate	7.9 ± 0.7[a]	23.8 ± 0.7[a]	(3.0 ± 0.2) x 10^6[a]	*Homo sapiens*	This work
	4.8 to 99			*Bos taurus*	[59,60]
	15 to 120			*Sus scrofa*	[59]
	90			*Oryctolagus cuniculus*	[59]
Isocitrate	100 ± 10[a]	14.1 ± 0.4[a]	(1.4 ± 0.1) x 10^5[a]	*Homo sapiens*	This work
	12 to 139			*Bos taurus*	[59,60]
	200 to 480			*Sus scrofa*	[59]
	320			*Oryctolagus cuniculus*	[59]
Citrate	950 ± 90[a]	10.2 ± 0.4[a]	(1.07 ± 0.06) x 10^4[a]	*Homo sapiens*	This work
	140 to 950			*Bos taurus*	[59,60]
	620 to 3600			*Sus scrofa*	[59]
	900			*Oryctolagus cuniculus*	[59]

[a] Values are mean ± SEM for 2 or 3 independent experiments. Constants were obtained by non-linear regression as recommended by Johnson, K. (2019) [61].

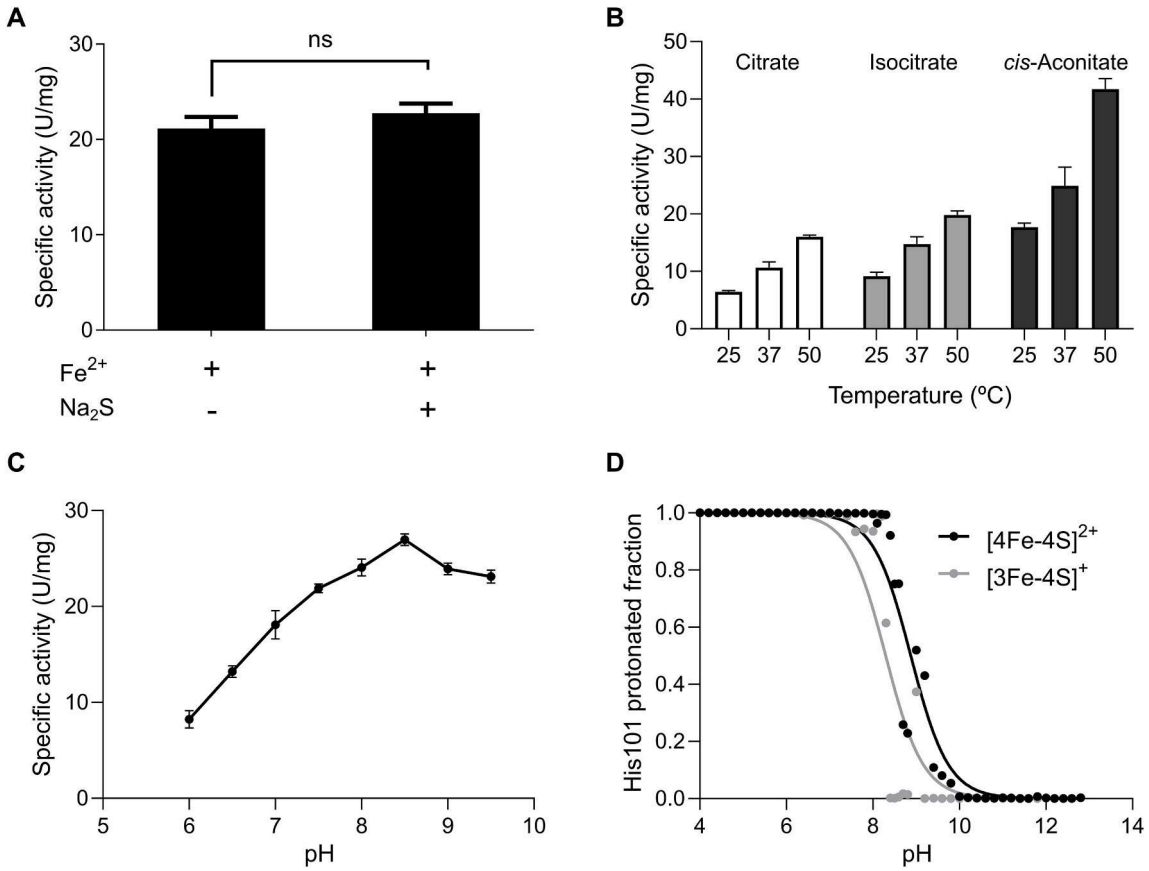

Fig. 2. *Biochemical characterization of ACO2.* A) ACO2 specific activity measured after a 1-h incubation under Ar atmosphere in presence of 100 μM Fe^{2+}, 10 mM DTT and 50 μM Na_2S. Measurements were repeated for three different protein batches. B) The ACO2 activity was measured at different temperatures using its three substrates after being previously equilibrated at the desired temperature using a spectrophotometer with a temperature-controlled Peltier and by following consumption or production of *cis*-aconitate. The substrate concentrations used were more than 10 K_M (10 mM citrate, 200 μM *cis*-aconitate, 1 mM isocitrate) and the concentration of ACO2 was 20 nM. C) Activity using 200 μM *cis*-aconitate was measured in buffer PIPES (pH 6.0 and 6.5), HEPES (pH 7.0 and 7.5), Tris-HCl (pH 8.0 to 9.5), 150 mM NaCl, at 25 °C. D) Titration curves for the catalytic His101 of ACO2 obtained by pHtMD. The Henderson-Hasselbalch equation was fitted to experimental data to obtain the pKa values (8.80 and 8.30 for the $[4Fe–4S]^{2+}$ and $[3Fe–4S]^{+}$ states of ACO2 respectively).

regarding the presence of sulfide, indicating that most freshly purified ACO2 is in the $[3Fe–4S]^{+}$ state.

To further characterize ACO2 kinetics, we studied the dependency between activity and temperature or pH under substrate saturation conditions. ACO2 activity showed to be dependent on the temperature up to 50 °C (Fig. 2B). At higher temperatures, ACO2 activity decreased and protein aggregation occurred as assessed by visual inspection and confirmed by SDS-PAGE (see below in Fig. 4). The optimal activity of ACO2 was reached at pH 8.5, similar to that reported for other mammalian aconitases [63] (Fig. 2C). The pKa of the catalytic His101 was estimated from simulated pHtMD titration curves, resulting in 8.80 and 8.30 for the $[4Fe–4S]^{2+}$ and $[3Fe–4S]^{+}$ states of ACO2 (Fig. 2D).

3.2. Reactivity of the human ACO2 with biologically relevant oxidants

As the Fe–S cluster of ACO2 is highly sensitive to oxidant species, we sought to determine the second-order constant rates for the reaction of ACO2 with several biologically relevant ROS. To avoid secondary reactions caused by reductants or free iron, excess iron and DTT added during activation were removed by molecular exclusion

chromatography before oxidants exposure.

To determine the $ONOO^-$ and $CO_3^{\bullet-}$ reaction constants, inactivation curves were simulated using GEPASI considering the reactions and constants already reported [10]. Experimental data best fitted rate constants in the order of 10^8 and 10^5 M^{-1} s^{-1} for $CO_3^{\bullet-}$ and $ONOO^-$ respectively (Fig. 3A and B).

The reaction constant with H_2O_2 was obtained by plotting the inactivation rates (k_{obs}) of ACO2 exposed to different H_2O_2 concentrations. The second-order rate constant for this reaction was in the order of 10^2 M^{-1} s^{-1} (Fig. 3C).

Finally, the reaction constant with $O_2^{\bullet-}$ was obtained by a simple competition assay for the oxidation of ACO2 in presence of a competitor (CuZnSOD) (Fig. 3D). Aconitase activity decreases in the presence of oxygen (filled circle) at a certain rate, while the presence of an $O_2^{\bullet-}$ and H_2O_2 generating system (empty triangle) increased this inactivation rate relative to both species alone, as the presence of only catalase (empty square) or SOD (filled triangle and empty circle) do not protect ACO2 completely. Complete protection is only achieved when catalase and SOD are added simultaneously (filled square). Under these conditions, the inactivation rate of aconitase is similar to the inactivation produced by oxygen alone. As there is no additional protection of SOD above 1.92 μM (filled square and filled triangle), it is reasonable to assume that the decrease in activity between the XO condition and the XO with 1.92 μM SOD lines represents 100% of $O_2^{\bullet-}$ mediated inactivation. This made it possible to apply Eq. (1) on the condition where there is XO and a SOD concentration (0.77 μM) which produces only partial inhibition of ACO2. The second-order rate constant reaction for the reaction of $O_2^{\bullet-}$ with active ACO2 obtained was (2.3 ± 0.8) x 10^8 M^{-1} s^{-1} at pH 8.4 and 25 °C.

All values obtained for the constant rates were similar to other values reported for other aconitases (Table 2). Altogether, the human ACO2 showed to be highly sensitive to biological oxidants as well as other bacterial and mammalian dehydratases. As with other ACO2 [10], the reactions with low oxidants concentrations were reversible as complete activity was achieved following incubation with DTT and Fe^{2+} for 1 h under an Ar-saturated atmosphere after inactivation by $O_2^{\bullet-}$, $ONOO^-$, $CO_3^{\bullet-}$ and H_2O_2 (Figure S-4).

3.3. Structural and dynamical characterization of ACO2

To investigate if the state (active $[4Fe–4S]^{2+}$ or inactive $[3Fe–4S]^{+}$) of the Fe–S cluster was important to the structure or stability of ACO2, we evaluated the thermal denaturation of the enzyme by following the intrinsic tryptophan fluorescence (9 residues) (Fig. 4). In the conformational transition between native and unfolded states, the fluorescence abruptly decreased with temperature as a result of the increased polarity of the Trp environment as they become exposed to solvent [66]. Denaturation curves for the $[4Fe–4S]^{2+}$ and $[3Fe–4S]^{+}$ states of ACO2 differed significantly being the $[4Fe–4S]^{2+}$ form more resistant to thermal denaturation as shown by the apparent-Tm (51 vs. 42.3 °C). For both states, the experiments were irreversible, and reducible high molecular weight aggregates appeared, therefore, thermodynamic parameters could not be obtained from these experiments (Fig. 4D). Differences in the denaturation curve of $ONOO^-$ treated ACO2 were also observed. At the concentration used (1 mM $ONOO^-$), ACO2 showed not only Fe–S oxidation but also other posttranslational oxidative modifications such as nitration and protein oligomerization [10,67] (confirmed herein, not shown).

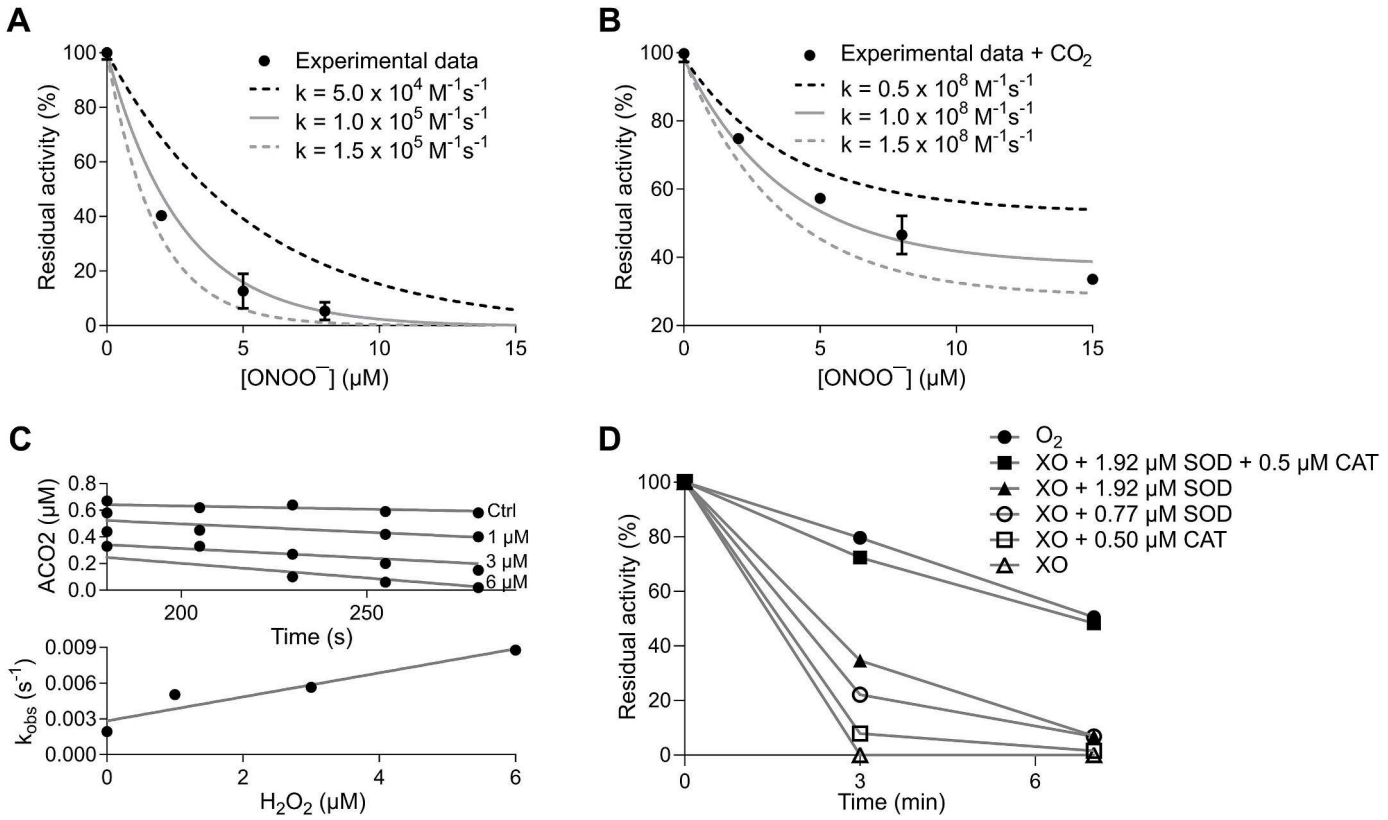

Fig. 3. *Second-order rate constants for the reactions of ACO2 with biologically relevant oxidants.* A-B) For $ONOO^-$ and $CO_3^{\bullet-}$, second-order rate constants with ACO2 were obtained after incubation of active ACO2 with a bolus addition of $ONOO^-$ in the absence (A) or presence (B) of 25 mM HCO_3^-. ACO2 inactivation was compared with simulated curves for the reaction considering different values for the reaction constant. C) To calculate the reaction rate constant with H_2O_2, active ACO2 was exposed to different concentrations of H_2O_2 (1, 3, and 6 μM) and activity was followed for 5 min. Inactivation rates were then plotted against H_2O_2 concentration to obtain the rate constant. D) Reaction rate constant for ACO2 inactivation by $O_2^{\bullet-}$ was obtained by a competition assay with Cu, Zn superoxide dismutase (SOD). ACO2 concentration in all experiments was in the range of 0.4–2 μM. For details see *Materials and methods*.

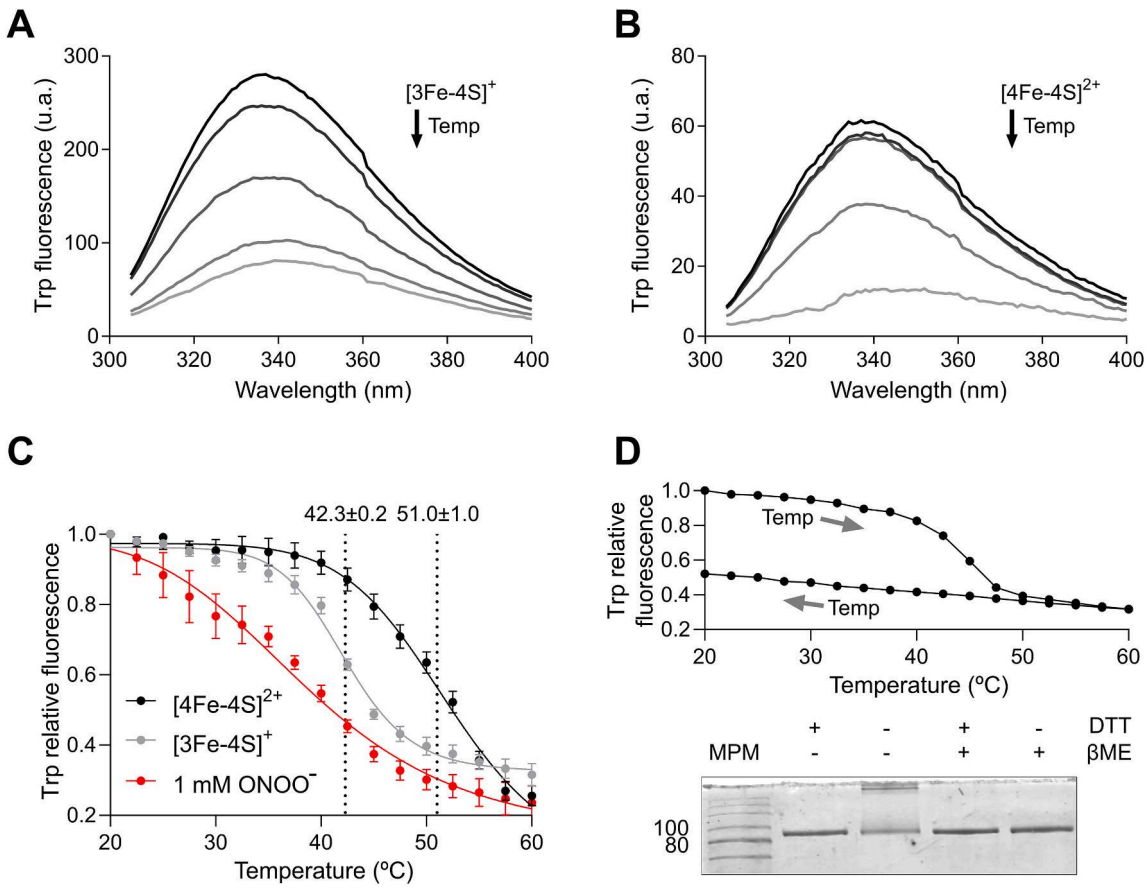

Fig. 4. *Temperature-induced unfolding comparison of the [4Fe–4S]$^{2+}$ and [3Fe–4S]$^{+}$ states of ACO2.* A-B) Intrinsic fluorescence emission spectra of thermally unfolded ACO2 at 10, 20, 30, 40, and 50 °C. The intrinsic fluorescence was measured with an excitation wavelength of 295 nm. C) Thermal-induced unfolding of ACO2. Unfolding curves were plotted by measuring the total area under spectra at each temperature. Points were connected to facilitate visualization. D) Assay showing the irreversibility of the unfolding. This was observed for all states of ACO2. Samples used on thermal unfolding assay were run on a 10% SDS-PAGE and stained with Coomassie blue. All assays were performed in a 20 mM HEPES buffer, pH 7.8 containing 100 mM NaCl and 2 μM ACO2.

Table 2
Second-order rate constants of ACO2 with biologically relevant oxidants.

Oxidant	Rate constant (M^{-1} s^{-1})	Organism	Reference
H_2O_2	(4.8 ± 2.9) x 10^2[a]	*Homo sapiens*	This work
	2 × 10^2	*E. coli*	[64]
$ONOO^-$	(0.9 ± 0.2) x 10^5[a]	*Homo sapiens*	This work
	(1.1 ± 0.2) x 10^5	*Sus scrofa*	[10]
	(1.4 ± 0.1) x 10^5		[6]
$CO_3^{\bullet-}$	(1.3 ± 0.3) x 10^8[a]	*Homo sapiens*	This work
	3 × 10^8	*Sus scrofa*	[10]
$O_2^{\bullet-}$	(2.3 ± 1.7) x 10^8[a]	*Homo sapiens*	This work
	3 × 10^7	*E. coli*	[65]
	0.8 × 10^7	*Sus scrofa*	[65]
	(3.5 ± 2) x 10^6		[6]
	(3 ± 2) x 10^6	*Bos taurus*	[64]

[a] Values are mean ± SEM for 3 or 4 independent experiments. Constants were obtained as explained in *Materials and methods.*

Titration assays with ANS showed that protein-ANS complex fluorescence is higher in the presence of inactive ACO2 than in the presence of active ACO2 (Fig. 5A). According to this result, analysis of the MD simulations of the [4Fe–4S]$^{2+}$ and inactive [3Fe–4S]$^{+}$ states showed a higher Solvent Accessible Surface Area (SASA) for the hydrophobic residues of ACO2 of about 400 Å^2 (Fig. 5B). The increase in the fluorescence intensity could be explained as an increase in the quantum yield of ANS, produced by a more hydrophobic environment, an increase in the number of ANS binding sites, or both.

The opening angle, measured as the angle formed by two groups of residues in antiparallel beta-sheets and centered in the Fe–S cluster differed in both states by about 27° (Fig. 5C). In 2 out of 3 replicas of 1 μs long MD simulations of the inactive ACO2, the model captured an "open" state, in comparison to the active ACO2 where this happened in 1 out of 6 replicas simulations and even when this occurred, the angle was of lesser magnitude. Analysis of the ACO2 cleft also showed an increased SASA in the [3Fe–4S]$^{+}$ inactive state (Fig. 5D). Concomitantly, the Fe–S cluster was much less solvated in the active state, implying that while in the active state, the Fe–S cluster is less solvent-exposed (Fig. 5E).

Therefore, ACO2 shows, as a dominant motion, closing-opening structural movements of the domains that comprise the active site, also known as a "breathing-like" motion, of higher magnitude when ACO2 is in the [3Fe–4S]$^{+}$ inactive state which exposes the cluster to the solvent. This might lead to the interaction with partners or be related to the ACO2 function as a redox "switch" (see below).

We also studied the interaction of ACO2 substrates at the active site employing MD simulations and MM-GBSA binding free energy estimations (Fig. 6A). Once restraints were completely removed, isocitrate stayed in the same binding mode, with little impact on the binding energy estimation. On the other hand, citrate (having a higher K_M), was displaced from starting conditions and final binding energy was higher, indicating a lesser affinity. Concomitantly, the substrate and active site residues mobility was significantly higher for citrate simulations than for isocitrate ones (Fig. 6B).

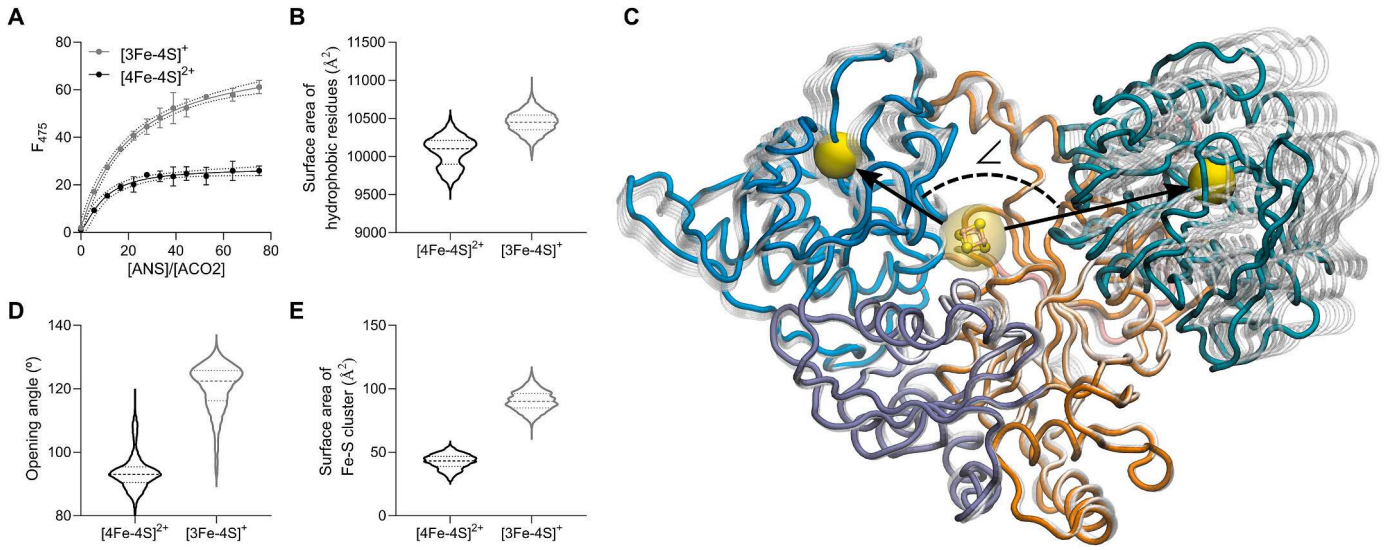

Fig. 5. *Comparison of dynamic characteristics of the [4Fe–4S]$^{2+}$ and [3Fe–4S]$^{+}$ states of ACO2.* A) ANS titration curves: fluorescence emission at 475 nm as a function of molar ratio [ANS]/ACO2 for active ([4Fe–4S]$^{2+}$) or inactive ([3Fe–4S]$^{+}$) ACO2. ANS fluorescence was measured at 20 °C using an excitation wavelength of 380 nm with ACO2 (4 μM) in HEPES 20 mM, pH 7.4. Respective buffer spectra were used for buffer subtraction. B) SASA of hydrophobic residues (Gly, Pro, Phe, Ala, Ile, Leu, Val, Met, Trp, Tyr) in the ([4Fe–4S]$^{2+}$ and [3Fe–4S]$^{+}$ states of ACO2. C) First non-trivial normal mode of ACO2 ("breathing-like" motion). ACO2 domains are colored as follows: domain 1, orange; domain 2, gray; domain 3, dark green; domain 4, cyan; hinge linker, pink. Fe–S cluster is represented along with two residue groups located on antiparallel beta sheets on domains 3 and 4 used as a reference for measuring the opening angle of ACO2 (yellow spheres). D) Opening angle of ACO2. E) Surface area of the Fe–S cluster for both states of ACO2.

3.4. ACO2-frataxin interaction

Fully active ACO2 was usually obtained in presence of Fe^{2+} and DTT after a 1-h incubation under an Ar-saturated atmosphere, while ACO2 reaches only less than 20% of maximum activity in the same conditions under air (21% O_2) (Fig. 7A).

To evaluate if Fe^{2+}-loaded FXN was able to activate ACO2 under air, we first preincubated FXN (6 μM) or BSA (2 mg/mL) with 300 μM Fe^{2+} in a 20 mM HEPES buffer containing 100 mM NaCl, pH 7.4 for 10 min. Then ACO2 and DTT were added to a final concentration of 1 μM and 10 mM respectively. Final FXN and Fe^{2+} concentrations were 4 μM and 200 μM. ACO2 activation was followed by taking aliquots and following the consumption of *cis*-aconitate at 240 nm. As shown in Fig. 7A the presence of FXN preloaded with Fe^{2+} promoted ACO2 reactivation *in vitro* under these conditions while BSA incubated with Fe^{2+} or Fe^{2+} alone did not have any effect on ACO2 activation, as previously shown for bovine ACO2 [20].

ACO2 (2 μM) was treated with 15 μM $ONOO^-$, a concentration shown to inactivate ACO2, in the presence or absence of 4 μM FXN (Fig. 7B). Under these conditions, FXN was unable to protect ACO2 from inactivation. On the other hand, aerobic reactivation of $ONOO^-$-treated ACO2 was obtained only in presence of iron-loaded FXN. As other biological oxidants such as $O_2^{\bullet-}$, H_2O_2 and $CO_3^{\bullet-}$ also promotes ACO2 inactivation by iron-sulfur cluster one-electron oxidation (reviewed in Ref. [68]), the effect of FXN promoting ACO2 reactivation is expected to be as for $ONOO^-$.

To determine if FXN is increasing the Fe^{2+} bioavailability for ACO2 reactivation or if there is a direct interaction between both proteins, a series of experiments were performed considering the conditions where we detected ACO2 activation by FXN (FXN preloaded with 300 μM Fe^{2+}, 10 mM DTT and 2 μM ACO2 under air).

ACO2 has 9 Trp (Trp166, Trp222, Trp241, Trp373, Trp455, Trp574, Trp603, Trp657, Trp765) residues while FXN has 3 (Trp155, Trp168, Trp173) and part of these are exposed to solvent and thus are sensitive to quenching. The fluorescence emission spectrum of mixed FXN:ACO2 solution at a molar ratio of 2.5:1 showed higher quenching than the sum of the experimental spectra of the individual proteins (3% vs 12%) which implies that both proteins could be getting close to each other and quenching their Trp (Fig. 7C and D). This effect was higher in presence of Fe^{2+}, suggesting that iron might be important for the interaction. These results were reproducible and a representative experiment is shown. Yet, the presence of FXN did not change the temperature-induced unfolding of ACO2, as assessed in Fig. 4C (not shown).

We performed UV–visible spectra of [3Fe–4S]$^{+}$-ACO2 (as it is purified) and after its incubation with Fe^{2+} and DTT in the presence or absence of FXN (Figure S-5). Iron-sulfur proteins are known to have broad and unfeatured bands in the UV–visible absorption spectra, produced by a large number of electronic transitions and the number of metal atoms [69]. As shown in Figure S-5, human ACO2 showed this type of signal. This result resembles the spectrum of pig ACO2 reported in Ref. [70]. Following a 1 h incubation in presence of Fe^{2+} and DTT, an increase in the overall spectrum was observed, an effect that was potentiated by the addition of FXN, reflecting the improvement in the formation of [4Fe–4S]$^{2+}$-ACO2 [62].

Interaction ELISA [53] was performed to further evaluate the existence of physical interaction between FXN and ACO2 (Fig. 7E). The molar concentration required for 50% maximal binding of FXN to immobilized ACO2, representative of the binding affinity (K_a), were (1.1 ± 0.9) and (10 ± 2) μM in conditions with and without Fe^{2+}, indicating a higher affinity of FXN for ACO2 when Fe^{2+} is present. The maximal binding (Fig. 7F), representing the coupling strength or the off-rate of the protein pair's binding, showed no differences concerning iron addition. Similar results were obtained from fluorescence anisotropy assays, a magnitude inversely related to the rotational mobility of a fluorescent molecule (Fig. 7G). We performed the addition of ACO2 to a cuvette containing 1 μM of a fluorescent Texas Red-labeled FXN in conditions where we observed ACO2 activation by FXN (in presence of Fe^{2+} and DTT). An increase in anisotropy was observed with the addition of ACO2 indicating the formation of a Texas Red-FXN:ACO2 complex. When non-labeled FXN was added, the anisotropy decreased as a result of an equilibrium displacement and the increase in free Texas Red-labeled FXN. In addition, as shown in Fig. 7H, in presence of Fe^{2+}, an increase in almost 0.008 anisotropy units was observed when adding 5 μM ACO2 to 1 μM TR-labeled FXN, while in absence of Fe^{2+}, adding 20 μM ACO2 increased the anisotropy in about 0.006 units. This implies that more ACO2 was needed to allow the formation of a complex in

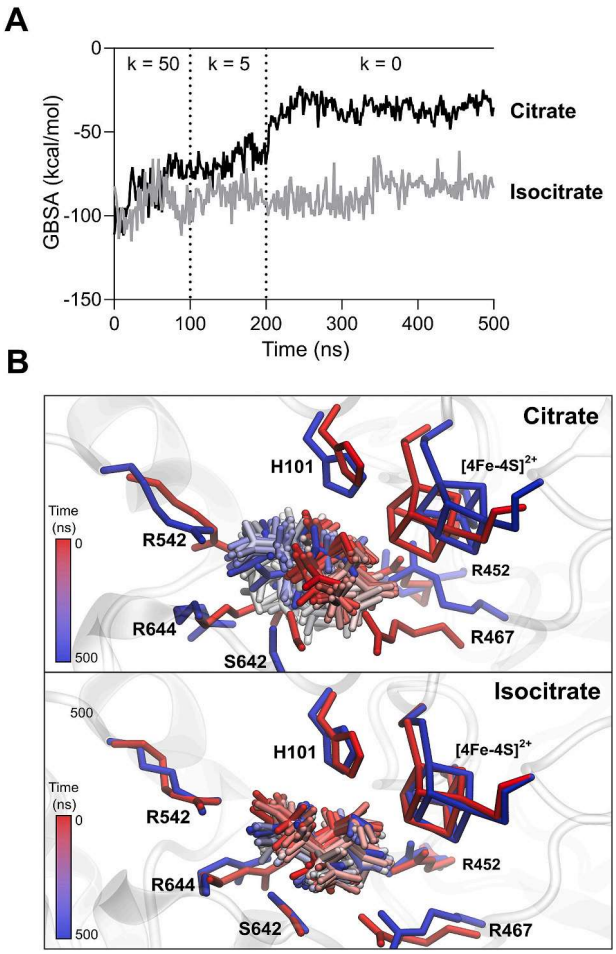

Fig. 6. *Substrate binding to ACO2.* A) MMGBSA-calculated binding energies of citrate and isocitrate with ACO2. Data based on 500 ns long simulation trajectories for the MD simulation. Harmonic restraint constants (k, kcal/mol) were changed at 100 and 200 ns allowing the binding modes to relax within the active site. B) Representation of the substrate binding to the active site of ACO2. For active site residues, only the first and last frames were represented, while for the substrate, 20 structures equally spaced in time are represented (from red: beginning of the trajectory, to blue: end of the trajectory).

absence of Fe^{2+}.

This data suggests that FXN directly interacts with ACO2 favored by the presence of Fe^{2+} and under these conditions; ACO2 is capable of regaining function.

To supplement the experimental data and provide further insight into the interaction, we developed a structural model for a 1:1 ACO2: FXN complex. As a first step, we used the AlphaFold-Multimer to generate models using the sequences of the human ACO2 and human FXN. As this tool considers data about the coevolution of the protein pair, we compared the predicted complexes of the WT proteins to the complexes of the proteins when the Glu and Asp acid residues from the acidic ridge region of FXN (known to contain iron-binding motifs [52]), were replaced by alanines (Figure S-6). The five predicted models for the WT complex were similar, as all of them had FXN located in the same region next to the ACO2 cleft formed between domains 3 and 4 (where the Fe–S cluster is located) and had the acidic ridge region oriented towards ACO2. On the other hand, when using the *in silico* mutated FXN, the models differed greatly in the FXN relative location with respect to ACO2, thus implying that the mutated acidic residues could be important for the interaction from a coevolutionary point of view. Prediction quality control indicators and the sequence coverage of the MSA are shown in Figure S-7.

Based on this information, we developed a docking model by defining as the active residues participating in the interaction, residues on the acidic ridge region of FXN, and residues on the ACO2 cleft (Fig. 8). As starting models of ACO2, we selected structures from the MD simulations that captured the "open" ($[3Fe–4S]^{+}$) and "closed" ($[4Fe–4S]^{2+}$) states of ACO2. The complex model for the "open" state of ACO2 shows FXN positioned inside the ACO2 cleft with the acidic ridge oriented to the Fe–S cluster to a distance of about 8 Å. In contrast, in the "closed" state, FXN was not capable of entering into the cleft and approaching the Fe–S cluster (22 Å), mainly because this state does not expose the Fe–S cluster. The replacement of the acidic residues of the acidic ridge by the non-polar amino acid Ala to the FXN did not greatly affect the complex structure but showed an increased HADDOCK score (less energy stability) in comparison with the WT complexes (Figure S-8).

4. Discussion

In this work, we successfully purified the human ACO2 for the first time to provide biochemical and structural data as well as presented robust evidence for its physical interaction with FXN.

Michaelis-Menten constants were higher with citrate, followed by isocitrate and *cis*-aconitate respectively (Fig. 1), as reported for other ACO2 (Table 1). Concomitantly, the binding energies obtained by MM-GBSA analysis showed a higher affinity of the ACO2 active site for the isocitrate with respect to citrate. This analysis was not done for *cis*-aconitate, as structural data for its binding mode was poorly defined (Fig. 6).

The Fe–S cluster of ACO2 has been reported to be very sensitive to various biological oxidants. In this regard, in the absence of protective substrates, human ACO2 was readily inactivated by $O_2^{\bullet-}$, $CO_3^{\bullet-}$, $ONOO^-$ and H_2O_2 (Fig. 3), showing inactivation second-order rate constants in the order of previously reported constants for other mammalian ACO2 (Table 2). This is consistent with the high conservation of the active site among species [2].

As for other mammalian ACO2, human ACO2 showed an optimal pH of around 8 (Fig. 2D), which is in line with the mitochondrial matrix pH. The catalytic His101 acts as an acid in the dehydration reaction by donating its proton to citrate or isocitrate [47]. For this to occur, His101 must be protonated. Considering a physiological pH in the mitochondrial matrix of 7.8 [71] and the results shown in Fig. 2C, about 90% of ACO2 has its His101 protonated in the $[4Fe–4S]^{2+}$ state, (while for the $[3Fe–4S]^{+}$ ACO2, is about 68%) which is in agreement with the reaction mechanism of ACO2 [47]. As this difference might not be significant, the pKa of His101 is higher than the reference value for the free His (6.00) [72] for both $[3Fe–4S]^{+}$ and $[4Fe–4S]^{2+}$ ACO2.

Maximal V_{max} for all substrates was achieved at 50 °C (Fig. 2A), the temperature at which mitochondria are proposed to be physiologically maintained [73]. Interestingly, thermal instability and aggregation of ACO2 were found to occur in intact mitochondria at 37 °C while complete aggregation was detected after incubation of isolated mitochondria at 45 °C, a condition where the majority of matrix proteins remain soluble [74]. This is in line with the irreversible thermal unfolding of ACO2 observed herein, but we detected differences between the $[3Fe–4S]^{+}$ and $[4Fe–4S]^{2+}$ states, as the inactive state promoted denaturation (lowered apparent-Tm) (Fig. 4). $ONOO^-$ treated ACO2 showed an even greater increase in its tendency for denaturation and aggregation.

In addition, increased ANS fluorescence was observed in the $[3Fe–4S]^{+}$ state (Fig. 5), suggesting a higher hydrophobic peptide region exposure which increases the probability of irregular protein-protein interaction, covalent crosslinking and aggregation. In mitochondria, aggregation of oxidatively modified ACO2 is prevented by its degradation by the Lon protease [75], activity that declines during senescence and aging [75,76]. The MD simulations showed an increased solvent exposure of hydrophobic residues for the $[3Fe–4S]^{+}$ state of ACO2

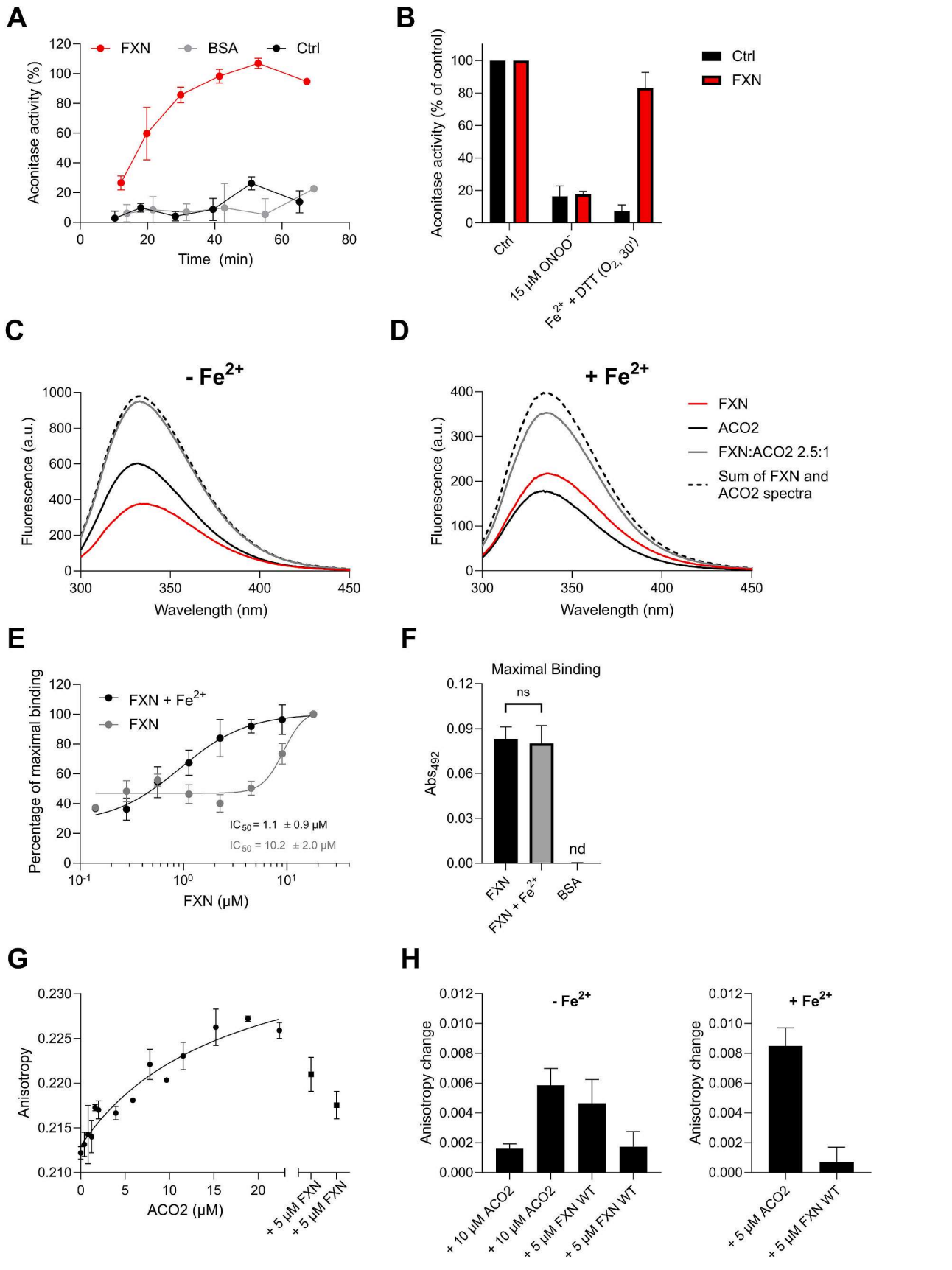

(caption on next page)

Fig. 7. *Interaction between ACO2 and FXN.* A) ACO2 activation assay. FXN 3.7 μM (1.2 mg/mL) or BSA 1.2 mg/mL were preincubated with 300 μM Fe^{2+} and then ACO2 and DTT were added to a final concentration of 1 μM and 10 mM respectively. Final Fe^{2+} concentration was 200 μM. Vial was left open and exposed to air and ACO2 activity was followed by taking aliquots and measuring the consumption of 200 μM *cis*-aconitate. B) Active aconitase was treated with $ONOO^-$ in the presence or absence of FXN. Reactivation of $ONOO^-$ treated ACO2 when sample was exposed to air occurred only in presence of FXN. C-D) Fluorescence emission spectra of ACO2 (2 μM) and FXN (5 μM) alone or in the same solution in the presence or absence of 200 μM Fe^{2+}; λ_{exc} = 280 nm. E) Normalized interaction curves obtained from an interaction ELISA for ACO2 and FXN. ACO2 was immobilized to the well and interaction was carried out in conditions where ACO2 activation by FXN was observed (in presence of Fe^{2+} and DTT or only DTT). Control wells had no ACO2 immobilized or BSA was used instead of FXN. No binding was detected when using BSA (nd). F) Maximal binding of the interaction ELISA. G) Direct binding curve obtained from a fluorescence anisotropy experiment measuring the binding of a fluorescent Texas Red-labeled FXN to ACO2 in the presence or absence of 200 μM Fe^{2+} and 10 mM DTT. The reversibility of binding was verified by adding non-labeled FXN in a 1:4,5 and 1:2.2 FXN:ACO2 ratio. H) Change of anisotropy by a single addition of ACO2 or non-labeled FXN in absence or presence of 200 μM Fe^{2+}. Non-labeled FXN was added in a 1:4 and 2:4 FXN:ACO2 ratio in abscence of Fe^{2+}, and 1:1 in presence of Fe^{2+}.

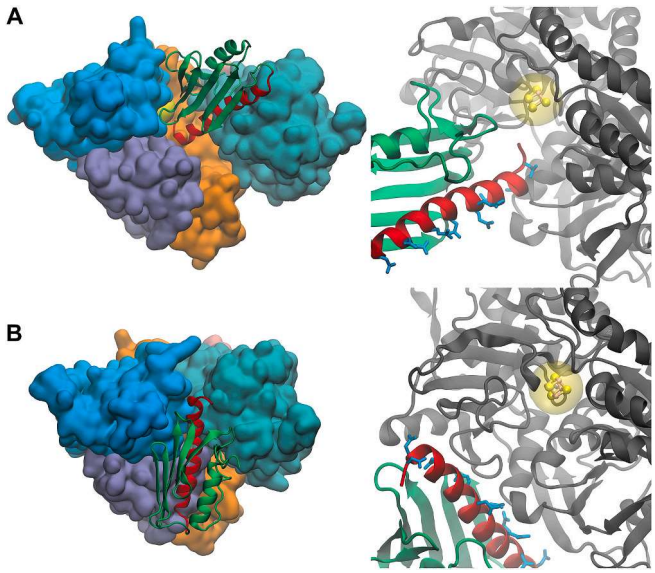

Fig. 8. *Proposed protein-protein interaction model of ACO2 and FXN.* Protein-protein docking model of WT human ACO2 (human ACO2 PDB based on 6ACN) and WT human FXN (PDB ID:1EKG) predicted with HADDOCK 2.4 Web Server. Starting ACO2 models were taken from the MD simulation for the inactive (A) or active (B) ACO2. Distance from the Fe–S cluster to the acidic ridge region of FXN is 8 Å in (A) and 22 Å in (B). ACO2 domains are colored as in Fig. 5. FXN is colored green with the acidic ridge region in red. In close-up representations, the glutamic and aspartic acid residues were colored cyan.

(Fig. 5B), supporting the experimental observation shown in Fig. 5A. In line with this result, normal mode analysis, measuring of opening angle and Fe–S cluster solvent exposition (Fig. 5C–E) support the existence of a "breathing-like" motion of ACO2, which might lead to conformations where substrate exchange or interaction with protein partners could be favored.

Under physiological conditions, ACO2 is in a steady state between the $[4Fe–4S]^{2+}$ and $[3Fe–4S]^{+}$ states, and approximately a 10–15% inactive fraction is present in bacteria and mammalian cells growing in normoxia [5,77]. Although the inactivation mechanism by oxidants is well known, the *in vivo* reactivation was not fully comprehended. For reactivation, ACO2 needs an electron (donated by ascorbic acid, glutathione, or cysteine, readily available in the mitochondria [78]), and a ferrous ion. The mitochondrial labile iron pool (LIP), used for Fe–S cluster and heme biosynthesis, is estimated to be around 0.5–10 μM in mammalian cells and has been suggested to be mostly in the ferrous state forming low M_r complexes (e.g., iron-citrate, iron-β-Citryl-L-glutamate) or bound to iron chaperones [79–81]. One of these iron chaperones' candidates for interacting with ACO2 is FXN [20]. Mutations or more frequently low expression of FXN are associated with the neurodegenerative disease Friedreich's ataxia (FRDA), whose phenotype is caused by depletion of Fe–S cluster-containing proteins, including ACO2 [82,83].

Herein we showed that iron-loaded human recombinant FXN was capable of activating the oxygen or $ONOO^-$ inactivated $[3Fe–4S]^{+}$-ACO2 (Fig. 7). In addition, we provide strong evidence for a direct iron-dependent interaction between FXN and ACO2.

For experimental purposes, we preferred to use FXN 90–210 because purification yield and protein stability are higher than FXN 81–210 (final mitochondrial processed protein), as residues 81 to 90 are disordered (reviewed in Ref. [84]). Nonetheless, we are aware that His86 is capable of coordinating iron and we could be underestimating mature FXN iron binding capacity [85].

Intrinsic fluorescence spectra for ACO2 and FXN alone or together in the same solution in presence of iron suggested a physical interaction between the proteins. As iron is a fluorescence quencher and might interfere with the assay, other approaches were used, including protein-protein interaction ELISA and fluorescence anisotropy which confirmed the iron-dependent interaction.

The ACO2-FXN docking complex with the $[3Fe–4S]^{+}$ state of ACO2 showed that FXN could get close enough for the iron atoms bound to the acidic ridge region, to physically diffuse to the inactive Fe–S cluster (Fig. 8) [86]. Interestingly, the ACO2-FXN model complex predicted by AlphaFold2-Multimer, which considered the coevolution of ACO2 and FXN was sensible to the *in silico* mutation of the Glu and Asp of the acidic ridge to Ala, showing the importance of these residues for the interaction (Figure S-2).

The supporting role of FXN on ACO2 activity has also been demonstrated in mice cardiomyocytes treated with doxorubicin that showed 50% reduced FXN expression, free iron accumulation increased mitochondrial ROS formation and 40% reduced ACO2 activity [87]. Also, HIF-2 α-knock-out mice livers which presented a reduced FXN expression (<50% of WT) showed a significant reduction in ACO2 activity (45%) even though ACO2 expression was higher than in WT) [88]. Moreover, in heart biopsies obtained from FRDA patients, ACO2 was the most affected activity among other Fe–S proteins suggesting that biosynthesis, as well as cluster reconstitution, might be compromised [82].

Recently, combining site-directed spin-labeling coupled with paramagnetic resonance and fluorescence quenching experiments as well as a molecular docking approach, revealed that human SOD2 (MnSOD) can interact with human FXN *in vitro*, in a complex that leaves the metal binding region accessible to the solvent [89]. This observation supports the hypothesis that a ternary complex among the three proteins could operate in the mitochondrial matrix or at least implies the relevancy of the interplay between these three proteins. Therefore, it can be assumed that ACO2 operates as a redox sensor due to the $O_2^{\bullet-}$ sensitivity and specificity of its reaction with the Fe–S cluster, and its interaction with FXN which promotes its reconstitution and bring together MnSOD to cope with $O_2^{\bullet-}$.

In summary, the present study describes for the first time the novel expression, purification, and characterization of recombinant human ACO2, including kinetics, oxidant reactivity, and dynamics, validating previous results inferred to human ACO2 from other mammalians homologous. In addition, we present various evidence for its direct interaction with FXN. Multimer modeling and protein-protein docking sustain an ACO2-FXN complex where the metal ion binding region of FXN approaches the $[3Fe–4S]^{+}$ cluster. This work confirmed that FXN

acts as a protein partner of ACO2 not only during Fe–S maturation but also in repairing oxidatively inactivated aconitase, supporting that highly compromised aconitase activity in FRDA in animal and cellular disease models may be the result of both the decrease of Fe–S cluster biosynthesis and the decrease in the ACO2 activation processes.

Acknowledgments

To Mauricio Mastrogiovanni, for his assistance with mass spectrometry measurements. To Julia Castroman, for English grammar and editing. Financial support for this work was received from: Comisión Sectorial de Investigación Científica (CSIC I + D 2020, ID23), Universidad de la República (UdelaR), Uruguay, CSIC grupos (767), UdelaR Espacio Interdisciplinario, Centros 2015, UdelaR, Programa de Desarrollo de las Ciencias Básicas (PEDECIBA), Uruguay to LC, VT and SM and Friedreich's Ataxia Research Alliance to JS. Fellowship has been granted by Comisión Académica de Posgrado (CAP), UdelaR, Uruguay to SM.

Appendix A. Supplementary data

Supplementary data to this article can be found online at https://doi.org/10.1016/j.freeradbiomed.2023.01.028.

References

[1] A.H. Robbins, C.D. Stout, The structure of aconitase, Proteins 5 (1989) 289–312, https://doi.org/10.1002/prot.340050406.
[2] H. Beinert, M.C. Kennedy, C.D. Stout, Aconitase as Iron−Sulfur protein, enzyme, and iron-regulatory protein, Chem. Rev. 96 (1996) 2335–2374, https://doi.org/10.1021/cr950040z.
[3] W.E. Walden, From bacteria to mitochondria: aconitase yields surprises, Proc. Natl. Acad. Sci. U.S.A. 99 (2002) 4138–4140, https://doi.org/10.1073/pnas.082108799.
[4] P.R. Gardner, I. Fridovichs, Superoxide Sensitivity of the Escherichia coli Aconitase, 1991, pp. 19328–19333, https://doi.org/10.1016/S0021-9258(18)55001-8.
[5] P.R. Gardner, I. Fridovich, Inactivation-reactivation of aconitase in Escherichia coli. A sensitive measure of superoxide radical, J. Biol. Chem. 267 (1992) 8757–8763, https://doi.org/10.1016/s0021-9258(19)50343-x.
[6] L. Castro, M. Rodriguez, R. Radi, Aconitase is readily inactivated by peroxynitrite, but not by its precursor, nitric oxide, J. Biol. Chem. 269 (1994) 29409–29415.
[7] L. a Castro, R.L. Robalinho, a Cayota, R. Meneghini, R. Radi, Nitric oxide and peroxynitrite-dependent aconitase inactivation and iron-regulatory protein-1 activation in mammalian fibroblasts, Arch. Biochem. Biophys. 359 (1998) 215–224, https://doi.org/10.1006/abbi.1998.0898.
[8] K.S. Aulak, M. Miyagi, L. Yan, K.A. West, D. Massillon, J.W. Crabb, D.J. Stuehr, Proteomic method identifies proteins nitrated in vivo during inflammatory challenge, Proc. Natl. Acad. Sci. U.S.A. 98 (2001) 12056–12061, https://doi.org/10.1073/pnas.221269198.
[9] K.S. Aulak, T. Koeck, J.W. Crabb, D.J. Stuehr, Dynamics of protein nitration in cells and mitochondria, Am. J. Physiol. Heart Circ. Physiol. 286 (2004) H30–H38, https://doi.org/10.1152/ajpheart.00743.2003.
[10] V. Tórtora, C. Quijano, B. Freeman, R. Radi, L. Castro, Mitochondrial aconitase reaction with nitric oxide, S-nitrosoglutathione, and peroxynitrite: mechanisms and relative contributions to aconitase inactivation, Free Radic. Biol. Med. 42 (2007) 1075–1088, https://doi.org/10.1016/j.freeradbiomed.2007.01.007.
[11] H.A. Krebs, The equilibrium constants of the fumarase and aconitase systems, Biochem. J. 54 (1953) 78–82. http://www.pubmedcentral.nih.gov/articlerender.fcgi?artid=1268849&tool=pmcentrez&rendertype=abstract.
[12] F. Scandroglio, V. Tórtora, R. Radi, L. Castro, Metabolic control analysis of mitochondrial aconitase: influence over respiration and mitochondrial superoxide and hydrogen peroxide production, Free Radic. Res. 48 (2014) 684–693, https://doi.org/10.3109/10715762.2014.900175.
[13] J.S. Armstrong, M. Whiteman, H. Yang, D.P. Jones, The redox regulation of intermediary metabolism by a superoxide-aconitase rheostat, Bioessays 26 (2004) 894–900, https://doi.org/10.1002/bies.20071.
[14] L.C. Costello, R. Franklin, R. Stacey, Mitochondrial isocitrate dehydrogenase and isocitrate oxidation of rat ventral prostate, Enzyme 21 (1976) 495–506, https://doi.org/10.1159/000458902.
[15] R.B. Franklin, L.C. Costello, The important role of the apoptotic effects of Zinc in the development of cancers, J. Cell. Biochem. 106 (2009) 750–757, https://doi.org/10.1002/jcb.22049.
[16] K.K. Singh, M.M. Desouki, R.B. Franklin, L.C. Costello, Mitochondrial aconitase and citrate metabolism in malignant and nonmalignant human prostate tissues, Mol. Cancer 5 (2006) 14, https://doi.org/10.1186/1476-4598-5-14.
[17] N. Westergaard, H.S. Waagepetersen, B. Belhage, A. Schousboe, Citrate, a ubiquitous key metabolite with regulatory function in the CNS, Neurochem. Res. 42 (2017) 1583–1588, https://doi.org/10.1007/s11064-016-2159-7.
[18] V. Iacobazzi, V. Infantino, Citrate-new functions for an old metabolite, Biol. Chem. 395 (2014) 387–399, https://doi.org/10.1515/hsz-2013-0271.
[19] T.A. Rouault, The role of iron regulatory proteins in mammalian iron homeostasis and disease, Nat. Chem. Biol. 2 (2006) 406–414, https://doi.org/10.1038/nchembio807.
[20] A. Bulteau, H.A. O'Neill, M.C. Kennedy, M. Ikeda-Saito, G. Isaya, L.I. Szweda, Frataxin acts as an iron chaperone protein to modulate mitochondrial aconitase activity, Science 305 (2004) 242–245, https://doi.org/10.1126/science.1098991 (80).
[21] N.G. Fox, X. Yu, X. Feng, H.J. Bailey, A. Martelli, J.F. Nabhan, C. Strain-Damerell, C. Bulawa, W.W. Yue, S. Han, Structure of the human frataxin-bound iron-sulfur cluster assembly complex provides insight into its activation mechanism, Nat. Commun. 10 (2019) 2210, https://doi.org/10.1038/s41467-019-09989-y.
[22] C.-L. Tsai, D.P. Barondeau, Human frataxin is an allosteric switch that activates the Fe−S cluster biosynthetic complex, Biochemistry 49 (2010) 9132–9139, https://doi.org/10.1021/bi1013062.
[23] J. Bridwell-Rabb, N.G. Fox, C.-L. Tsai, A.M. Winn, D.P. Barondeau, Human frataxin activates Fe–S cluster biosynthesis by facilitating sulfur transfer chemistry, Biochemistry 53 (2014) 4904–4913, https://doi.org/10.1021/bi500532e.
[24] T.A. Rouault, Biogenesis of iron-sulfur clusters in mammalian cells: new insights and relevance to human disease, DMM Dis. Model. Mech. 5 (2012) 155–164, https://doi.org/10.1242/dmm.009019.
[25] M. Nair, S. Adinolfi, C. Pastore, G. Kelly, P. Temussi, A. Pastore, Solution structure of the bacterial frataxin ortholog, CyaY, Structure. 12 (2004) 2037–2048, https://doi.org/10.1016/j.str.2004.08.012.
[26] J.D. Cook, K.Z. Bencze, A.D. Jankovic, A.K. Crater, C.N. Busch, P.B. Bradley, A. J. Stemmler, M.R. Spaller, T.L. Stemmler, Monomeric yeast frataxin is an iron-binding protein, Biochemistry 45 (2006) 7767–7777, https://doi.org/10.1021/bi060424r.
[27] M. Bellanda, L. Maso, D. Doni, M. Bortolus, E. De Rosa, F. Lunardi, A. Alfonsi, M. E. Noguera, M.G. Herrera, J. Santos, D. Carbonera, P. Costantini, Exploring iron-binding to human frataxin and to selected Friedreich ataxia mutants by means of NMR and EPR spectroscopies, Biochim. Biophys. Acta, Proteins Proteomics 1867 (2019), 140254, https://doi.org/10.1016/j.bbapap.2019.07.007.
[28] D.S. Vazquez, W.A. Agudelo, G. Ferrer-Sueta, L. Giraudo, M.C. González Lebrero, M. Aran, J. Santos, Remodelling the surface of thioredoxin from Escherichia coli by grafting an iron-binding site from the CyaY protein family, Dalton Trans. 51 (2022) 17587–17601, https://doi.org/10.1039/D2DT02599J.
[29] K. Cai, R.O. Frederick, M. Tonelli, J.L. Markley, Interactions of iron-bound frataxin with ISCU and ferredoxin on the cysteine desulfurase complex leading to Fe-S cluster assembly, J. Inorg. Biochem. 183 (2018) 107–116, https://doi.org/10.1016/j.jinorgbio.2018.03.007.
[30] S. Schmucker, A. Martelli, F. Colin, A. Page, M. Wattenhofer-Donzé, L. Reutenauer, H. Puccio, Mammalian frataxin: an essential function for cellular viability through an interaction with a preformed ISCU/NFS1/ISD11 iron-sulfur assembly complex, PLoS One 6 (2011) 1–12, https://doi.org/10.1371/journal.pone.0016199.
[31] A. Pastore, H. Puccio, Frataxin: a protein in search for a function, J. Neurochem. 126 (2013) 43–52, https://doi.org/10.1111/jnc.12220.
[32] R. Radi, J.S. Beckman, K.M. Bush, B.A. Freeman, Peroxynitrite oxidation of sulfhydryls. The cytotoxic potential of superoxide and nitric oxide, J. Biol. Chem. 266 (1991) 4244–4250. http://www.ncbi.nlm.nih.gov/pubmed/1847917.
[33] A.C. Varela, R. Pikielny, N. Balbi, S. Faraj, J. Santos, Ferrari, Desarrollo de un sistema de cuantificación de frataxina humana para el diagnóstico complementario y seguimiento de individuos con Ataxia de Friedreich, Rev. Bioquímica Y Patol. Clínica. 82 (2021) 11–21. http://www.revistabypc.org.ar/index.php/bypc/article/view/83.
[34] Steve Rozen, J. Helen, Skaletsky, Bioinformatics Methods and Protocols: Methods in Molecular Biology, Humana Press, Totowa, NJ, 2000.
[35] M.C. Kennedy, M.H. Emptage, J.L. Dreyer, H. Beinert, M.H. Emptageg, J. Dreyerll, H. Beinert, M.H. Emptage, J.L. Dreyer, H. Beinert, The role of iron in the activation-inactivation of aconitase, J. Biol. Chem. 258 (1983) 11098–11105. http://www.ncbi.nlm.nih.gov/pubmed/6309829.
[36] H. Shintani, Oxygen uptake and spectrophotometric measurement of Superoxide, Hydrogen peroxide and hydroxyl radicals, Pharm. Anal. Acta (2013), https://doi.org/10.4172/2153-2435.S7-005, 01.
[37] I. Fridovich, Superoxide radical: an endogenous toxicant, Annu. Rev. Pharmacol. Toxicol. 23 (1983) 239–257, https://doi.org/10.1146/annurev.pa.23.040183.001323.
[38] J. Schymkowitz, J. Borg, F. Stricher, R. Nys, F. Rousseau, L. Serrano, The FoldX web server: an online force field, Nucleic Acids Res. 33 (2005) W382–W388, https://doi.org/10.1093/nar/gki387.
[39] E. Krieger, G. Vriend, YASARA View—molecular graphics for all devices—from smartphones to workstations, Bioinformatics 30 (2014) 2981–2982, https://doi.org/10.1093/bioinformatics/btu426.
[40] D.J. Price, C.L. Brooks, A modified TIP3P water potential for simulation with Ewald summation, J. Chem. Phys. 121 (2004) 10096–10103, https://doi.org/10.1063/1.1808117.
[41] A.T.P. Carvalho, M. Swart, Electronic structure investigation and parametrization of biologically relevant iron–sulfur clusters, J. Chem. Inf. Model. 54 (2014) 613–620, https://doi.org/10.1021/ci400718m.
[42] D.J.F.M.J. Frisch, G.W. Trucks, H.B. Schlegel, G.E. Scuseria, M.A. Robb, J. R. Cheeseman, G. Scalmani, V. Barone, G.A. Petersson, H. Nakatsuji, X. Li, M. Caricato, A. Marenich, J. Bloino, B.G. Janesko, R. Gomperts, B. Mennucci, H. P. Hratchian, J.V. Ort, Gaussian09, Revision A (2016), 02, https://gaussian.com/citation/.

[43] L.F. Song, T.-S. Lee, C. Zhu, D.M. York, K.M. Merz, Using AMBER18 for relative free energy calculations, J. Chem. Inf. Model. 59 (2019) 3128–3135, https://doi.org/10.1021/acs.jcim.9b00105.
[44] J. Mongan, D.A. Case, Biomolecular simulations at constant pH, Curr. Opin. Struct. Biol. 15 (2005) 157–163, https://doi.org/10.1016/j.sbi.2005.02.002.
[45] J. Mongan, D.A. Case, J.A. McCammon, Constant pH molecular dynamics in generalized Born implicit solvent, J. Comput. Chem. 25 (2004) 2038–2048, https://doi.org/10.1002/jcc.20139.
[46] G. Rastelli, A. Del Rio, G. Degliesposti, M. Sgobba, Fast and accurate predictions of binding free energies using MM-PBSA and MM-GBSA, J. Comput. Chem. 32 (2009), https://doi.org/10.1002/jcc.21372. NA-NA.
[47] S.J. Lloyd, H. Lauble, G.S. Prasad, C.D. Stout, The mechanism of aconitase: 1.8 A resolution crystal structure of the S642a:citrate complex, Protein Sci. 8 (1999) 2655–2662, https://doi.org/10.1110/ps.8.12.2655.
[48] D.R. Roe, T.E. Cheatham, PTRAJ and CPPTRAJ: software for processing and analysis of molecular dynamics trajectory data, J. Chem. Theor. Comput. 9 (2013) 3084–3095, https://doi.org/10.1021/ct400341p.
[49] B.J. Grant, A.P.C. Rodrigues, K.M. ElSawy, J.A. McCammon, L.S.D. Caves, Bio3d: an R package for the comparative analysis of protein structures, Bioinformatics 22 (2006) 2695–2696, https://doi.org/10.1093/bioinformatics/btl461.
[50] W. Humphrey, A. Dalke, K. Schulten, VMD: visual molecular dynamics, J. Mol. Graph. 14 (1996) 33–38, https://doi.org/10.1016/0263-7855(96)00018-5.
[51] E.A. Roman, S.E. Faraj, M. Gallo, A.G. Salvay, D.U. Ferreiro, J. Santos, Protein stability and dynamics modulation: the case of human frataxin, PLoS One 7 (2012), https://doi.org/10.1371/journal.pone.0045743.
[52] M.F. Pignataro, M.G. Herrera, N. Fernández, M. Aran, F. Bataglini, J. Santos, Selection of synthetic proteins to modulate the human frataxin function, bioRxiv (2022) 2022, 02.11.480108, http://biorxiv.org/content/early/2022/02/12/2022.02.11.480108.abstract.
[53] B.J. Biesiadecki, J.-P. Jin, A high-throughput solid-phase microplate protein-binding assay to investigate interactions between myofilament proteins, J. Biomed. Biotechnol. 2011 (2011) 1–8, https://doi.org/10.1155/2011/421701.
[54] J.R. Lakowicz (Ed.), Principles of Fluorescence Spectroscopy, Springer US, Boston, MA, 2006, https://doi.org/10.1007/978-0-387-46312-4.
[55] A. Gijsbers, T. Nishigaki, N. Sánchez-Puig, Fluorescence anisotropy as a tool to study protein-protein interactions, JoVE 2016 (2016) 1–9, https://doi.org/10.3791/54640.
[56] M. Mirdita, K. Schütze, Y. Moriwaki, L. Heo, S. Ovchinnikov, M. Steinegger, ColabFold: making protein folding accessible to all, Nat. Methods 19 (2022) 679–682, https://doi.org/10.1038/s41592-022-01488-1.
[57] C. Dominguez, R. Boelens, A.M.J.J. Bonvin, HADDOCK: a Protein−Protein docking approach based on biochemical or biophysical information, J. Am. Chem. Soc. 125 (2003) 1731–1737, https://doi.org/10.1021/ja026939x.
[58] G.C.P. van Zundert, J.P.G.L.M. Rodrigues, M. Trellet, C. Schmitz, P.L. Kastritis, E. Karaca, A.S.J. Melquiond, M. van Dijk, S.J. de Vries, A.M.J.J. Bonvin, The HADDOCK2.2 web server: user-friendly integrative modeling of biomolecular complexes, J. Mol. Biol. 428 (2016) 720–725, https://doi.org/10.1016/j.jmb.2015.09.014.
[59] J.P. Glusker, Aconitase, in: Paul D. Boyer (Ed.), Enzym., the Enzymes, Academic Press, 1971, pp. 413–439, https://doi.org/10.1016/S1874-6047(08)60097-9.
[60] J.V. Schloss, W.W. Cleland, M.H. Emptage, pH profiles and isotope effects for aconitases from saccharomycopsis lipolytica, beef heart, and beef liver. α-Methyl-czs-aconitate and threo-Ds-α-Methylisocitrate as substrates, Biochemistry 23 (1984) 4572–4580, https://doi.org/10.1021/bi00315a010.
[61] K.A. Johnson, New standards for collecting and fitting steady state kinetic data, Beilstein J. Org. Chem. 15 (2019) 16–29, https://doi.org/10.3762/bjoc.15.2.
[62] M.C. Kennedy, H. Beinert, The state of cluster SH and S2-of aconitase during cluster interconversions and removal. A convenient preparation of apoenzyme, J. Biol. Chem. 263 (1988) 8194–8198.
[63] J.F. Morrison, The influence of buffers on the pH optimum of aconitase, Aust. J. Exp. Biol. Med. Sci. 32 (1954) 877–883, https://doi.org/10.1038/icb.1954.91.
[64] D.H. Flint, J.F. Tuminello, M.H. Emptage, The inactivation of Fe-S cluster containing hydro-lyases by superoxide, J. Biol. Chem. 268 (1993) 22369–22376. http://www.ncbi.nlm.nih.gov/pubmed/8226748.
[65] A. Hausladen, I. Fridovichs, Superoxide and peroxynitrite inactivate aconitases, but nitric oxide does not, J. Biol. Chem. 269 (1994) 29405–29408.
[66] P.M. Froehlich, M. Yeats, The effect of mixed aqueous solvent systems on the fluorescence of indoles and aromatic amino acids and their metabolites, Anal. Chim. Acta 87 (1976) 185–191, https://doi.org/10.1016/S0003-2670(01)83134-2.
[67] D. Han, R. Canali, J. Garcia, R. Aguilera, T.K. Gallaher, E. Cadenas, Sites and mechanisms of aconitase inactivation by peroxynitrite: modulation by citrate and glutathione, Biochemistry 44 (2005) 11986–11996, https://doi.org/10.1021/bi0509393.
[68] L. Castro, V. Tórtora, S. Mansilla, R. Radi, Aconitases: non-redox iron-sulfur proteins sensitive to reactive species, Acc. Chem. Res. 52 (2019) 2609–2619, https://doi.org/10.1021/acs.accounts.9b00150.
[69] I.O. Betinol, S. Nader, S.S. Mansy, Spectral decomposition of iron-sulfur clusters, Anal. Biochem. 629 (2021), 114269, https://doi.org/10.1016/j.ab.2021.114269.
[70] D. Piszkiewicz, O. Gawron, J.C. Sutherland, Analysis of the iron-sulfur cluster of aconitase by natural and magnetic circular dichroism, Biochemistry 20 (1981) 363–366, https://doi.org/10.1021/bi00505a021.
[71] A.M. Porcelli, A. Ghelli, C. Zanna, P. Pinton, R. Rizzuto, M. Rugolo, pH difference across the outer mitochondrial membrane measured with a green fluorescent protein mutant, Biochem. Biophys. Res. Commun. 326 (2005) 799–804, https://doi.org/10.1016/j.bbrc.2004.11.105.
[72] D.R. Lide, Handbook of Chemistry and Physics, 103rd ed., 2022. Boca Raton, https://hbcp.chemnetbase.com/faces/contents/ContentsSearch.xhtml;jsessionid=AD04F6DEBD1B8104F112DCD276A3E91F.
[73] D. Chrétien, P. Bénit, H.-H. Ha, S. Keipert, R. El-Khoury, Y.-T. Chang, M. Jastroch, H.T. Jacobs, P. Rustin, M. Rak, Mitochondria are physiologically maintained at close to 50 °C, PLoS Biol. 16 (2018), e2003992, https://doi.org/10.1371/journal.pbio.2003992.
[74] A. Wilkening, C. Rüb, M. Sylvester, W. Voos, Analysis of heat-induced protein aggregation in human mitochondria, J. Biol. Chem. 293 (2018) 11537–11552, https://doi.org/10.1074/jbc.RA118.002122.
[75] J.K. Ngo, L.C.D. Pomatto, D.A. Bota, A.L. Koop, K.J.A. Davies, Impairment of lon-induced protection against the accumulation of oxidized proteins in senescent wi-38 fibroblasts, J. Gerontol. A. Biol. Sci. Med. Sci. 66 (2011) 1178–1185, https://doi.org/10.1093/gerona/glr145.
[76] D.A. Bota, K.J.A. Davies, Lon protease preferentially degrades oxidized mitochondrial aconitase by an ATP-stimulated mechanism, Nat. Cell Biol. 4 (2002) 674–680, https://doi.org/10.1038/ncb836.
[77] P.R. Gardner, I. Raineri, L.B. Epstein, C.W. White, Superoxide radical and iron modulate aconitase activity in mammalian cells, J. Biol. Chem. 270 (1995) 13399–13405, https://doi.org/10.1074/jbc.270.22.13399.
[78] S.R. Dickman, A.A. Cloutier, Factors affecting the activity of aconitase, J. Biol. Chem. 188 (1951) 379–388.
[79] N.D. Jhurry, M. Chakrabarti, S.P. McCormick, G.P. Holmes-Hampton, P.A. Lindahl, Biophysical investigation of the ironome of human jurkat cells and mitochondria, Biochemistry 51 (2012) 5276–5284, https://doi.org/10.1021/bi300382d.
[80] M. Hamada-Kanazawa, M. Narahara, M. Takano, K.S. Min, K. Tanaka, M. Miyake, BETA.-Citryl-L-glutamate acts as an iron carrier to activate aconitase activity, Biol. Pharm. Bull. 34 (2011) 1455–1464, https://doi.org/10.1248/bpb.34.1455.
[81] D.R. Richardson, D.J.R. Lane, E.M. Becker, M.L.H. Huang, M. Whitnall, Y. S. Rahmanto, A.D. Sheftel, P. Ponka, Mitochondrial iron trafficking and the integration of iron metabolism between the mitochondrion and cytosol, Proc. Natl. Acad. Sci. U.S.A. 107 (2010) 10775–10782, https://doi.org/10.1073/pnas.0912925107.
[82] A. Rötig, P. de Lonlay, D. Chretien, F. Foury, M. Koenig, D. Sidi, A. Munnich, P. Rustin, Aconitase and mitochondrial iron–sulphur protein deficiency in Friedreich ataxia, Nat. Genet. 17 (1997) 215–217, https://doi.org/10.1038/ng1097-215.
[83] R.A. Vaubel, G. Isaya, Iron-sulfur cluster synthesis, iron homeostasis and oxidative stress in Friedreich ataxia, Mol. Cell. Neurosci. 55 (2013) 50–61, https://doi.org/10.1016/j.mcn.2012.08.003.
[84] I.H. Castro, M.F. Pignataro, K.E. Sewell, L.D. Espeche, M.G. Herrera, M.E. Noguera, L. Dain, A.D. Nadra, M. Aran, C. Smal, M. Gallo, J. Santos, Frataxin Structure and Function, 2019, pp. 393–438, https://doi.org/10.1007/978-3-030-28151-9_13.
[85] L.E. Gentry, M.A. Thacker, R. Doughty, R. Timkovich, L.S. Busenlehner, His86 from the N - terminus of frataxin coordinates iron and is required for Fe, S Cluster Synthesis (2013), https://doi.org/10.1021/bi400443n.
[86] J. Buffle, Z. Zhang, K. Startchev, Metal flux and dynamic speciation at (Bio) interfaces. Part I: critical evaluation and compilation of physicochemical parameters for complexes with simple ligands and fulvic/humic substances, Environ. Sci. Technol. 41 (2007) 7609–7620, https://doi.org/10.1021/es070702p.
[87] X. Fu, M. Eggert, S. Yoo, N. Patel, J. Zhong, I. Steinke, M. Govindarajulu, E. A. Turumtay, S. Mouli, P. Panizzi, R. Beyers, T. Denney, R. Arnold, R.H. Amin, The cardioprotective mechanism of phenylaminoethyl selenides (PAESe) against doxorubicin-induced cardiotoxicity involves frataxin, Front. Pharmacol. 11 (2021), https://doi.org/10.3389/fphar.2020.574656.
[88] Y. Oktay, E. Dioum, S. Matsuzaki, K. Ding, L.-J. Yan, R.G. Haller, L.I. Szweda, J. A. Garcia, Hypoxia-inducible factor 2α regulates expression of the mitochondrial aconitase chaperone protein frataxin, J. Biol. Chem. 282 (2007) 11750–11756, https://doi.org/10.1074/jbc.M611133200.
[89] D. Doni, M. Meggiolaro, J. Santos, G. Audran, S.R.A. Marque, P. Costantini, M. Bortolus, D. Carbonera, A combined spectroscopic and in silico approach to evaluate the interaction of human frataxin with mitochondrial superoxide dismutase, Biomedicines 9 (2021) 1763, https://doi.org/10.3390/biomedicines9121763.